The Astronomical Journal, 160:259 (19pp), 2020 December https://doi.org/10.3847/1538-3881/abbe19

A Mini-Neptune and a Radius Valley Planet Orbiting the Nearby M2 Dwarf TOI-1266 in Its Venus Zone: Validation with the Habitable-zone Planet Finder

Guðmundur Stefánsson[1,21], Ravi Kopparapu[2], Andrea Lin[3,4], Suvrath Mahadevan[3,4], Caleb I. Cañas[3,4,22], Shubham Kanodia[3,4], Joe P. Ninan[3,4], William D. Cochran[5,6], Michael Endl[5,6], Leslie Hebb[7], John Wisniewski[8], Arvind Gupta[3,4], Mark Everett[9], Chad F. Bender[10], Scott A. Diddams[11,12], Eric B. Ford[3,4,13], Connor Fredrick[11,12], Samuel Halverson[14,15,23], Fred Hearty[3,4], Eric Levi[3,4], Marissa Maney[3], Andrew J. Metcalf[11,12,16], Andrew Monson[3,4], Lawrence W. Ramsey[3,4], Paul Robertson[17], Arpita Roy[18,24], Christian Schwab[19], Ryan C. Terrien[20], and Jason T. Wright[3,4]

[1] Princeton University, Department of Astrophysical Sciences, 4 Ivy Lane, Princeton, NJ 08540, USA; gstefansson@astro.princeton.edu
[2] NASA Goddard Space Flight Center, 8800 Greenbelt Road, Greenbelt, MD 20771, USA
[3] Department of Astronomy & Astrophysics, The Pennsylvania State University, 525 Davey Laboratory, University Park, PA 16802, USA
[4] Center for Exoplanets and Habitable Worlds, 525 Davey Laboratory, University Park, PA 16802, USA
[5] McDonald Observatory and Department of Astronomy, The University of Texas at Austin, 2515 Speedway, Austin, TX 78712, USA
[6] Center for Planetary Systems Habitability, The University of Texas at Austin, 2515 Speedway, Austin, TX 78712, USA
[7] Department of Physics, Hobart and William Smith Colleges, 300 Pulteney Street, Geneva, NY 14456, USA
[8] Homer L. Dodge Department of Physics and Astronomy, University of Oklahoma, 440 West Brooks Street, Norman, OK 73019, USA
[9] NSF's OIR Lab, 950 North Cherry Avenue, Tucson, AZ 85719, USA
[10] Steward Observatory, The University of Arizona, 933 North Cherry Avenue, Tucson, AZ 85721, USA
[11] Time and Frequency Division, National Institute of Standards and Technology, 325 Broadway, Boulder, CO 80305, USA
[12] Department of Physics, University of Colorado, 2000 Colorado Avenue, Boulder, CO 80309, USA
[13] Institute for Computational & Data Sciences, University Park, PA 16802, USA
[14] MIT Kavli Institute for Astrophysics, 70 Vassar Street, Cambridge, MA 02109, USA
[15] Jet Propulsion Laboratory, 4800 Oak Grove Drive, Pasadena, CA 91109, USA
[16] Space Vehicles Directorate, Air Force Research Laboratory, 3550 Aberdeen Avenue SE, Kirtland AFB, NM 87117, USA
[17] Department of Physics and Astronomy, The University of California, Irvine, Irvine, CA 92697, USA
[18] Department of Astrophysics, California Institute of Technology, Pasadena, CA 91125, USA
[19] Department of Physics and Astronomy, Macquarie University, Balaclava Road, North Ryde, NSW 2109, Australia
[20] Department of Physics and Astronomy, Carleton College, One North College Street, Northfield, MN 55057, USA

Received 2020 June 18; revised 2020 September 24; accepted 2020 September 25; published 2020 November 13

Abstract

We report on the validation of two planets orbiting the nearby (36 pc) M2 dwarf TOI-1266 observed by the TESS mission. This system is one of a few M dwarf multiplanet systems with close-in planets where the inner planet is substantially larger than the outer planet. The inner planet is sub-Neptune-sized ($R = 2.46 \pm 0.08\ R_{\oplus}$) with an orbital period of 10.9 days, while the outer planet has a radius of $1.67^{+0.09}_{-0.11}\ R_{\oplus}$ and resides in the exoplanet radius valley—the transition region between rocky and gaseous planets. With an orbital period of 18.8 days, the outer planet receives an insolation flux of 2.4 times that of Earth, similar to the insolation of Venus. Using precision near-infrared radial velocities with the Habitable-zone Planet Finder Spectrograph, we place upper mass limits of 15.9 and 6.4 $M_{\oplus}$ at 95% confidence for the inner and outer planet, respectively. A more precise mass constraint of both planets, achievable with current radial velocity instruments given the host star brightness ($V = 12.9$, $J = 9.7$), will yield further insights into the dominant processes sculpting the exoplanet radius valley.

Unified Astronomy Thesaurus concepts: Exoplanets (498); Cold Neptunes (2132); Mini Neptunes (1063); Super Earths (1655); Extrasolar rocky planets (511); Exoplanet detection methods (489); Transit photometry (1709)

Supporting material: data behind figure, machine-readable table

1. Introduction

One of the key findings from the Kepler mission (Borucki et al. 2010) is that planets with radii between Earth (1 $R_{\oplus}$) and Neptune (4 $R_{\oplus}$)—which are not known to exist in the solar system—are prevalent (e.g., Howard et al. 2012; Batalha et al. 2013; Fressin et al. 2013; Petigura et al. 2013; Dressing & Charbonneau 2015). In this grouping of planets, Kepler data further showed convincing evidence that there is a dip in the radius distribution of Kepler planets at 1.5–2.0 $R_{\oplus}$ (Owen & Wu 2013; Fulton et al. 2017; Fulton et al. 2018; Van Eylen et al. 2018; Petigura 2020). This gap, or "radius valley," has been interpreted as the transition between predominantly rocky planets (super-Earths) populating the space below the gap and planets rich in volatiles or ices residing above the gap (sub-Neptunes). Subsequent studies have found evidence of the radius valley in the K2 mission (Hardegree-Ullman et al. 2020) and explored how it varies as a function of stellar type (e.g., Cloutier & Menou 2020).

The astrophysical origin of the radius valley has been explored by a number of groups (see, e.g., Owen & Wu 2013; Lee et al. 2014; Owen & Wu 2017; Lopez & Rice 2018). Different theoretical models predict that the location of the rocky-to-gaseous transition radius should depend on the planet orbital period. First, the photoevaporation model (Lopez et al. 2012; Lopez & Fortney 2013; Owen & Wu 2013, 2017)—where a planet's primordial atmosphere is stripped by X-ray

---

[21] Henry Norris Russell Fellow.
[22] NASA Earth and Space Science Fellow.
[23] Sagan Fellow.
[24] Robert A. Millikan Postdoctoral Fellow.

and ultraviolet (XUV) photons from the host star—predicts that the rocky-to-gaseous transition radius should decrease with orbital period (as $\sim P^{-0.15}$). Second, internally driven thermal atmospheric escape models via the core-powered mass-loss mechanism (Ginzburg et al. 2016, 2018; Gupta & Schlichting 2019) also predict that the location of the radius valley should decrease with orbital period (as $\sim P^{-0.13}$). Third, giant impacts can also provide a way to sculpt the atmospheric properties of small planets and strip large primordial envelopes down to a few percent by mass (Inamdar & Schlichting 2015; Liu et al. 2015; Wyatt et al. 2020). Conversely, models assuming formation at later times in a gas-poor environment (Lee et al. 2014; Lee & Chiang 2016; Lopez & Rice 2018) predict that the location of the radius valley should increase with period (as $\sim P^{0.11}$).

Knowledge of planetary bulk densities—and thus planetary compositions—as a function of orbital period offers a direct observational test of the predictions of the different hypotheses mentioned above. However, the current number of planets with precise bulk density constraints is insufficient to robustly identify the dominant formation pathway of the radius valley (Cloutier & Menou 2020). The Transiting Exoplanet Survey Satellite (TESS; Ricker et al. 2015), which is surveying the night sky for transiting exoplanets around the nearest and brightest stars, is finding more planets amenable to precise mass measurements.

We report on the discovery and ground-based validation of two small exoplanets orbiting the nearby M dwarf TOI-1266 observed in four sectors of TESS data. The inner planet has a period of $P = 10.9$ days and radius of $R = 2.46 \pm 0.08\ R_\oplus$ and likely has a gaseous envelope. The outer planet has a period of $P = 18.8$ days and radius of $R = 1.67^{+0.09}_{-0.11}\ R_\oplus$ and thus resides in the exoplanet radius valley, and it could either have retained a small gaseous envelope or have a predominantly rocky composition. Receiving insolation fluxes of $4.7^{+1.0}_{-0.7}$ and $2.42^{+0.23}_{-0.22} S_\oplus$, both planets reside in the exoplanet "Venus zone"—the region between the runaway greenhouse boundary defined by Kopparapu et al. (2013) and 25 $S_\oplus$ (Kane et al. 2014; Ostberg & Kane 2019)—where the outer planet has an insolation flux similar to that of Venus of 1.91 $S_\oplus$. The detailed characterization of systems in the Venus zone, including mass and atmospheric compositions, will increase our understanding of the limits of habitable environments. Venus-zone planets are not necessarily Venus analogs. They also include planets in a transition state to hot/moist rich atmospheres or undergoing runaway greenhouse. Some of these climate states can be potentially observed in transits through their radius inflation resulting from the runaway greenhouse (Turbet et al. 2019). Observing these transition climate states provides an empirical evaluation of the habitable-zone limits and corresponding validation of the climate models that assess the habitability of terrestrial planets. Using precise radial velocities from the Habitable-zone Planet Finder (HPF) Spectrograph, we place upper limits on the mass of both planets. Both planets are amenable for mass constraints with additional radial velocity (RV) observations. A mass constraint of the outer planet will allow its composition to be determined and will be a valuable data point in discerning between competing models explaining the emergence of the radius valley.

This paper is structured as follows. Section 2 describes the observations and data reduction. In Section 3, we describe the key parameters of the host star, and in Section 4, we describe our constraints on the parameters of the planets. In Section 5, we statistically validate both planets. In Section 6, we place the TOI-1266 system in context with other exoplanet systems, and we conclude in Section 7 with a summary of our key findings.

2. Observations and Data Reduction

2.1. TESS Photometry

TESS observed TOI-1266 in four sectors: sector 14 (camera 4; 2019 July 18–2019 August 15), sector 15 (camera 4; 2019 August 15–2019 September 11), sector 21 (camera 3; 2020 January 21–2020 February 18), and sector 22 (camera 3; 2020 February 18–2020 March 18). In the TESS Input Catalog (TIC; Stassun et al. 2018, 2019), TOI-1266 is listed as TIC 467179528. Pixel data in an 11 × 11 array surrounding TOI-1266 were averaged into 2 minute stacks, which were reduced to light curves by the Science Processing Operations Center (SPOC) at NASA Ames (Jenkins et al. 2016). We analyzed the presearch data conditioning single-aperture photometry (PDCSAP) light curve, which contains systematics-corrected data using the algorithms originally developed for the Kepler data analysis pipeline. The PDCSAP light curve uses pixels chosen to maximize the signal-to-noise ratio (S/N) of the target and has removed systematic variability by fitting out trends common to many stars (Smith et al. 2012; Stumpe et al. 2014). Figure 1 highlights the TESS apertures for the different TESS sectors and nearby stars detected by Gaia. From Figure 1, we see that two stars partially overlap the TESS apertures for TOI-1266 (Tmag = 11.0) in some sectors: TIC 467179527 (Tmag = 15.6; separation of 36″) and TIC 467179526 (Tmag = 18.338; separation of 36″), both of which are significantly fainter (ΔTmag = 4.6 and 7.3) than TOI-1266. The faintness and separation of the two stars results in minimal dilution of the TESS light curve.

Analysis by the TESS SPOC identified two possible planetary signals, and human vetting of the data reports (Twicken et al. 2018; Li et al. 2019) resulted in the announcement of planet candidates TOI-1266.01 and TOI-1266.02, available on the TESS alerts website.[25] The SPOC data validation reports (Twicken et al. 2018; Liu et al. 2019) note no significant centroid offsets for either planet candidate.

To clean the available TESS data, we removed all points with nonzero quality flags (4844 in total), which indicate known problems (e.g., Tenenbaum & Jenkins 2018). We removed an additional 12 points that we identified as 4σ outliers (two lower outliers and 10 upper outliers; the upper outliers were not suggestive of stellar flares), leaving a total of 68,891 points that we used for the fitting, with a median error bar of 2270 ppm. The median-normalized TESS PDCSAP light curve is shown in Figure 2. We retrieved the data using the `lightkurve` package (Lightkurve Collaboration et al. 2018).

2.2. Ground-based Photometry with the 0.4 m Perkin Telescope

We observed a transit of TOI-1266b (Figure 2) on the night of 2020 March 21 using the 0.43 m (17″) Richard S. Perkin Telescope at Hobart and William Smith Colleges. The telescope is a 17″ PlaneWave Corrected Dall-Kirkham (CDK) telescope on a Paramount equatorial mount with an SBIG 8300 M camera with 3326 × 2504 pixels that are 5.4 × 5.4 μm square. The plate scale of the camera in the 1 × 1 binning mode we used is 0.″38 pixel^{-1},

---

[25] https://tev.mit.edu/data/

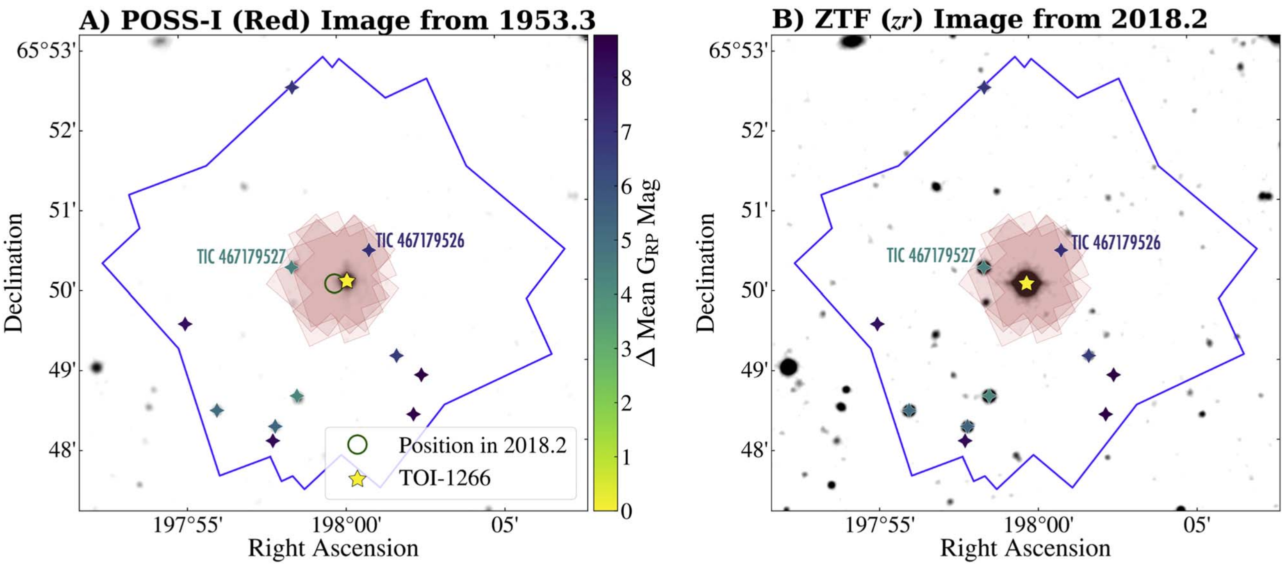

Figure 1. TESS apertures (red shaded areas) and full TESS 11 × 11 pixel grids (blue lines) highlighted over seeing-limited images from (a) POSS-1 from 1955.3 and (b) the ZTF (Masci et al. 2019) from 2018.2. The location of TOI-1266 is noted by the yellow star. Other nearby stars as detected by Gaia are highlighted with the color bar. Two nearby stars that are partially overlapping with the TESS aperture are highlighted, but due to their faintness, they result in minimal dilution of the TESS light curve. The green circle in panel (a) highlights the position of TOI-1266 in 2018, showing no evidence of an overlapping background star at its position during the TESS observations.

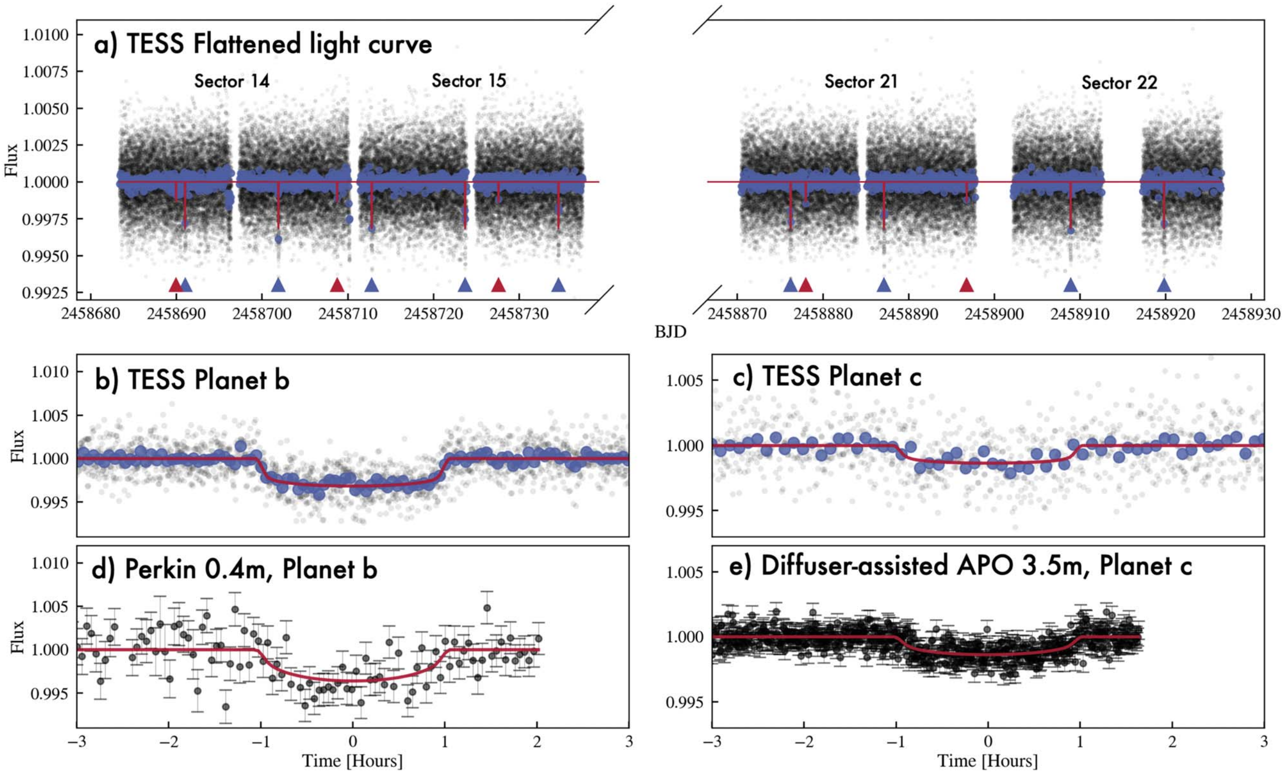

Figure 2. Transit photometry of TOI-1266. (a) Short-cadence (2 minute) TESS photometry is shown in black. The blue points show the data binned to 10 minutes. The red curve shows our best-fit joint model including both planets b and c. The blue and red triangles denote transits of planets b and c, respectively. (b) and (c) Phase-folded photometry from TESS of the transits of TOI-1266b and TOI-1266c, respectively. (d) Ground-based photometry from the 0.4 m Perkin Telescope showing the transit of TOI-1266b. (e) Diffuser-assisted photometry during the transit of TOI-1266c using the engineered diffuser on the 3.5 m telescope at APO.

(The data used to create this figure are available.)

resulting in a field of view (FOV) of $21' \times 16'$. We obtained 106 images over ∼5 hr centered on the target in the Sloan r' filter, where all images were taken above an airmass of 1.5. To improve the observing efficiency, we defocused moderately, which allowed us to use an exposure time of 180 s. The guiding was stable throughout the observations.

We processed the observations using AstroImageJ (Collins et al. 2017) using standard bias, dark, and flat-field frames. For flat-field calibrations, we used a median-combined flat created from 28 sky-flat images at the beginning of the observations. We performed aperture photometry using AstroImageJ (Collins et al. 2017) on the calibrated images. We systematically tested a number of different apertures from 15 to 30 pixels. Ultimately, we settled on an aperture of 18 pixels (6.″8) in radius with inner and outer sky annuli of 35 (13.″3) and 45 pixels (17.″1), respectively, which showed the lowest scatter in the final light curve. We experimented with detrending with different parameters (e.g., airmass, centroid offsets), but we observed no significant improvement in the resulting photometry.

2.3. Diffuser-assisted Photometry with the 3.5 m ARC Telescope

We observed a transit of TOI-1266c (Figure 2) on the night of 2020 January 28 using the Astrophysical Research Consortium Telescope Imaging Camera (ARCTIC) Imager (Huehnerhoff et al. 2016) on the 3.5 m Astrophysical Research Consortium (ARC) 3.5 m telescope at Apache Point Observatory (APO). The target rose from an airmass of 1.44 at the start of the observations to a minimum airmass of 1.19 and ended at a slightly lower airmass of 1.21. We observed the transit using the engineered diffuser available on ARCTIC, which we designed specifically to enable precision photometric observations from the ground on nearby bright stars (see, e.g., Stefansson et al. 2017, 2018a, 2018b, 2020a). The observations were performed using the Sloan Digital Sky Survey (SDSS) i' filter with an exposure time of 25 s in quad-readout mode with 4×4 on-chip binning. In this mode, ARCTIC has a gain of 2.0 e ADU^{-1}, a plate scale of 0.″44 pixel^{-1}, and a short readout time of 2.7 s.

We processed the data using AstroImageJ (Collins et al. 2017) using standard bias and dark frames. We did observe a linear trend in the data that, through visual inspection, could effectively be removed using a combination of detrending with a simultaneous line + airmass detrend. We experimented with reducing the photometry both with and without a flat-field calibration, but neither removed the observed trend. We saw a slight improvement in the resulting photometry without using the flat field, and as such, we elected to present the data without the flat-field calibration. As discussed below, for our final parameter estimation, we fit for the transit model simultaneously with a Gaussian process model using a Matern 3/2 kernel to account for this red-noise component observed in the transit data. Clear outliers, due to either cosmic rays or charged-particle events, were removed using AstroImageJ. To arrive at the final photometric reduction, we experimented with extracting the data using a number of different apertures and selected an aperture of 18 pixels (8″) with an inner sky annulus of 20 pixels (9″) and outer sky annulus of 50 pixels (22″), as this setting showed the overall lowest scatter in the final light curve.

2.4. HPF

We obtained high-resolution spectra of TOI-1266 with the HPF Spectrograph to place upper limits on the masses of both planets and obtain precise spectroscopic parameters of the host star. The HPF is a fiber-fed near-infrared (NIR) spectrograph on the 10 m Hobby-Eberly Telescope (HET; Mahadevan et al. 2012, 2014) at McDonald Observatory in Texas, covering the z, Y, and J bands from 810 to 1260 nm at a resolution of $R = 55{,}000$. To enable precision radial velocities in the NIR, the HPF is temperature-stabilized at the milli-Kelvin level (Stefansson et al. 2016). The HET is a fully queue-scheduled telescope (Shetrone et al. 2007), and all observations were executed as part of the HET queue. In total, we obtained 46 spectra in 22 different HET tracks[26] with two 969 s exposures taken, on average, in each HET track. The 46 different spectra had a median S/N of 135 per extracted 1D pixel evaluated at 1 μm and a median RV error bar of 10.3 m s^{-1}. After binning to the 22 different individual tracks, the median RV error bar is 7.4 m s^{-1}. We used the binned RVs for all subsequent analyses.

The HPF has an NIR laser frequency comb (LFC) calibrator to provide a precise wavelength solution and track instrumental drifts that has been shown to enable ∼20 cm s^{-1} RV calibration precision in 10 minute bins (Metcalf et al. 2019). Following Stefansson et al. (2020a), we elected not to use the simultaneous LFC calibration during the observations to minimize the risk of contaminating the science spectrum from scattered light from the LFC. Instead, we perform the RV drift correction by extrapolating the wavelength solution from LFC frames taken as part of standard evening/morning calibrations and from LFC calibration frames taken periodically throughout the night. This methodology has been shown to enable precise wavelength calibration at the ∼30 cm s^{-1} level, much smaller than the RV error bar of the observations discussed here.

The HPF 1D spectra were reduced using the HPF pipeline following the procedures in Ninan et al. (2018), Kaplan et al. (2018), and Metcalf et al. (2019). Following the 1D spectral extraction, we reduced the HPF radial velocities using an adopted version of the SpEctrum Radial Velocity Analyzer (`SERVAL`) pipeline (Zechmeister et al. 2018), which is described in Stefansson et al. (2020a). In short, `SERVAL` uses the template-matching algorithm to derive RVs, which has been shown to be particularly effective at producing precise radial velocities for M dwarfs (Anglada-Escudé & Butler 2012). `SERVAL` uses the `barycorrpy` package (Kanodia & Wright 2018), which uses the methodology of Wright & Eastman (2014) to calculate accurate barycentric velocities. Following Metcalf et al. (2019) and Stefansson et al. (2020a), we only use the eight HPF orders that are cleanest of tellurics, covering the wavelength regions 8540–8890 and 9940–10760 Å. We subtracted the estimated sky background from the stellar spectrum using the dedicated HPF sky fiber. Again following the methodology described in Metcalf et al. (2019) and Stefansson et al. (2020a), we explicitly masked out telluric and sky-emission lines to minimize their impact on the RV determination. Table 4 in Appendix B lists the RVs from the HPF used in this work.

2.5. Speckle Imaging

To rule out nearby companions, on the night of 2019 December 5, we obtained speckle observations of TOI-1266 using the NASA Exoplanet Star and Speckle Imager (NESSI; Scott et al. 2018) on the 3.5 m WIYN Telescope at Kitt Peak National Observatory in Arizona. We reduced the data following the methodologies outlined in Howell et al. (2011). NESSI provides a resolution of ∼0.″04 in two bands centered around 562 nm (width of 44 nm) and 832 nm (width of 40 nm; Scott et al. 2018). Figure 3 shows the resulting contrast curves

---

[26] The HET is a fixed-altitude telescope and can only observe a given target at certain times or "tracks."

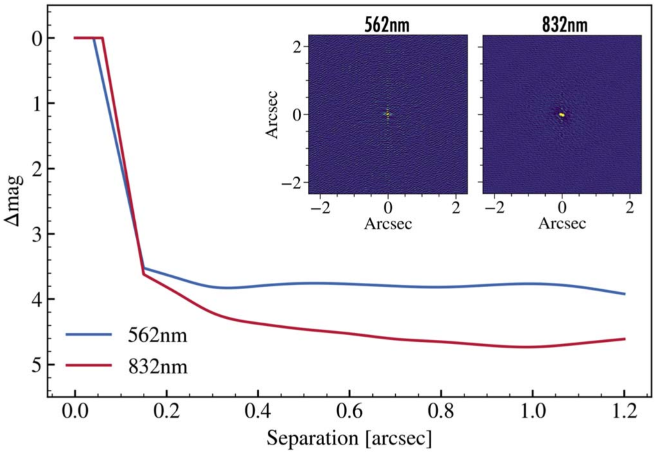

Figure 3. Contrast limits from our NESSI speckle imaging data shown in two different bands centered around 562 (blue) and 832 (red) nm. The insets show reconstructed images from the two bandpasses. No secondary sources are detected.

and reconstructed 256 × 256 images for the two bands. No secondary sources were detected in the reconstructed images, and from the contrast curve, we place a limit of Δmag ∼ 4 for nearby companions between $0\overset{''}{.}2$ and $1\overset{''}{.}2$.

3. Stellar Parameters

To obtain spectroscopic constraints on the effective temperature T_{eff}, stellar surface gravity $\log g$, and metallicity [Fe/H], we use the empirical spectral matching algorithm described in Stefansson et al. (2020a). In short, this algorithm closely follows the methodology in Yee et al. (2017), where the target spectrum is compared to a library of high-S/N as-observed spectra using a χ^2 metric. From our analysis of the HPF spectra, we obtain the following spectroscopic values: $T_{\mathrm{eff}} = 3563 \pm 77$ K, $\log g = 4.785 \pm 0.05$, and $[\mathrm{Fe/H}] = -0.121 \pm 0.13$. From the spectral matching analysis, the two best-matching stars are GJ 2066 and GJ 393, both of which have literature spectral types of M2.0 (see Alonso-Floriano et al. 2015 and Lépine et al. 2013, respectively), which we adopt for TOI-1266.

To obtain model-dependent constraints on the stellar mass, radius, effective temperature, and age, we fit the spectral energy distribution (SED) of TOI-1266 using the `EXOFASTv2` package (Eastman et al. 2019) using as inputs (a) the available literature photometry, (b) the Gaia distance from Bailer-Jones et al. (2018), and (c) the spectroscopic values discussed above as Gaussian priors. We adopt a uniform prior for the visual extinction where the upper limit is determined from estimates of Galactic dust by Green et al. (2019; Bayestar19) calculated at the distance determined by Bailer-Jones et al. (2018). We adopt the $R_v = 3.1$ reddening law from Fitzpatrick (1999) to convert the Bayestar19 extinction to a visual magnitude extinction. `EXOFASTv2` uses the BT-NextGen model grid of theoretical spectra (Allard et al. 2012) and the MESA Isochrones and Stellar Tracks (MIST; Choi et al. 2016; Dotter 2016) to fit the SED and derive model-dependent stellar parameters. Table 1 lists the resulting model-dependent stellar parameters derived from the SED analysis, which agree well with the spectroscopically derived parameters. We calculate the galactic U, V, and W velocities of TOI-1266 using the `GALPY` (Bovy 2015) package (see Table 1), and we note that Carrillo et al. (2020) calculated membership probabilities of 97.2%, 0.0%, and 2.8% for TOI-1266 to be a member of the galactic thin disk, thick disk, and halo populations, respectively.

From the spectral matching analysis, we also obtain a limit on the projected stellar rotational velocity of $v \sin i < 2$ km s^{-1}, suggestive of a slow rotator. This is in agreement with the fact that we do not see clear rotational modulation in the TESS photometry at short periods. As a further test, we analyzed available ground-based photometry from the All-Sky Automated Survey for SuperNovae (ASAS-SN; Kochanek et al. 2017) and the Zwicky Transient Facility (ZTF; Masci et al. 2019). We see no significant rotation signals that occur in both data sets by studying the Lomb–Scargle (LS) periodograms of these data sets. In addition, in Section 4.1, we discuss periodograms of activity indicators from the HPF spectra, which show no clear evidence of activity (e.g., no clear variability seen in the Ca II infrared triplet (Ca II IRT) or differential line widths (dLWs)). As such, without a clear indication of photometric modulation in either the TESS or the ground-based photometry or signs of activity from the HPF spectra, we conclude that TOI-1266 is an inactive star with a moderate or long rotation period.

4. Planet Parameters

4.1. Search for Additional Planets

We looked for additional transiting planets in the TESS data using the box least-squares (BLS) algorithm (Kovács et al. 2002) as implemented in the `lightkurve` package. Figure 4 shows the BLS power spectra of the available TESS photometry after iteratively masking out the transits of planets b and c (in a region 1.5 times as wide as the transit duration for each planet centered around the transit midpoints), showing no significant evidence for further transiting planets in the system. As an additional test, we tried looking for periodic transits using the transit least-squares algorithm (Hippke & Heller 2019) as implemented in the `transitleastsquares` package, which is optimized for detecting shallow periodic transits. In doing so, we see no clear signs of high-S/N transits with a signal detection efficiency (SDE) >15 as reported by the `transitleastsquares` code that were not driven by instrumental variations and/or other systematics close to the edges of the TESS sectors.

Some compact M dwarf multiplanet systems show significant transit timing variations (TTVs; Agol et al. 2005; Holman & Murray 2005) through gravitational interactions that occur when planets orbit close to mean-motion resonances (MMRs), including, e.g., the TRAPPIST-1 (Gillon et al. 2017) and K2-146 (Lam et al. 2020) systems. Such systems could have formed in a disk resulting in largely coplanar orbits where the planets obtained MMR orbits through convergent migration. To look for evidence of TTVs in the TOI-1266 system, we used the `TTVOrbit` fitting tools available in the `exoplanet` code (Foreman-Mackey et al. 2020). Although the period ratio of the two transiting TOI-1266 planets of $18.802/10.895 = 1.726$ is not close to a low-integer period ratio (e.g., $5/3 = 1.67$, $7/4 = 1.75$), which suggests that the two planets are not orbiting close to an MMR, there is a possibility that the two planets could be in MMR with potentially other nontransiting planets in the system. From our `exoplanet TTVOrbit` transit fits, we see no evidence for significant TTVs, and with all individual transit times fully consistent with a linear ephemeris, we conclude that there are no massive planets in

Table 1
Summary of Stellar Parameters Used in This Work

Parameter	Description	Value	Reference
Main Identifiers			
TIC	⋯	467179528	TIC
TOI	⋯	1266	TIC
2MASS	⋯	J13115955 + 6550017	TIC
Equatorial Coordinates, Proper Motion, and Spectral Type			
$\alpha_{\rm J2000}$	R.A.	13:11:59.18	Gaia
$\delta_{\rm J2000}$	decl.	+65:50:01.31	Gaia
μ_α	Proper motion (R.A., mas $\rm yr^{-1}$)	-150.652 ± 0.041	Gaia
μ_δ	Proper motion (decl., mas $\rm yr^{-1}$)	-25.368 ± 0.039	Gaia
Spectral type	⋯	M2	This work
Equatorial Coordinates, Proper Motion, and Spectral Type			
B	APASS Johnson B mag	14.578 ± 0.048	APASS
V	APASS Johnson V mag	12.941 ± 0.049	APASS
g'	APASS Sloan g' mag	13.811 ± 0.050	APASS
r'	APASS Sloan r' mag	12.297 ± 0.070	APASS
i'	APASS Sloan i' mag	11.246 ± 0.150	APASS
TESS-mag	TESS magnitude	11.040 ± 0.007	TIC
J	2MASS J mag	9.706 ± 0.023	2MASS
H	2MASS H mag	9.065 ± 0.030	2MASS
K_S	2MASS K_S mag	8.840 ± 0.020	2MASS
WISE1	WISE1 mag	8.715 ± 0.022	WISE
WISE2	WISE2 mag	8.612 ± 0.019	WISE
WISE3	WISE3 mag	8.504 ± 0.024	WISE
WISE4	WISE4 mag	8.233 ± 0.207	WISE
Spectroscopic Parameters[a]			
$T_{\rm eff}$	Effective temperature in K	3563 ± 77	This work
[Fe/H]	Metallicity in dex	-0.121 ± 0.13	This work
$\log(g)$	Surface gravity in cgs units	4.785 ± 0.05	This work
Model-dependent Stellar SED and Isochrone Fit Parameters[b] (Adopted)			
$T_{\rm eff}$	Effective temperature in K	3573^{+35}_{-38}	This work
[Fe/H]	Metallicity in dex	$-0.08^{+0.13}_{-0.10}$	This work
$\log(g)$	Surface gravity in cgs units	$4.826^{+0.020}_{-0.021}$	This work
M_*	Mass in $M_\odot$	0.437 ± 0.021	This work
R_*	Radius in $R_\odot$	$0.4232^{+0.0077}_{-0.0079}$	This work
ρ_*	Density in g $\rm cm^{-3}$	$8.13^{+0.47}_{-0.46}$	This work
Age	Age in Gyr	$7.9^{+4.2}_{-5.2}$	This work
L_*	Luminosity in $L_\odot$	$0.02629^{+0.00071}_{-0.00075}$	This work
A_v	Visual extinction in mag	$0.015^{+0.011}_{-0.010}$	This work
d	Distance in pc	$36.011^{+0.029}_{-0.030}$	Gaia, Bailer-Jones
π	Parallax in mas	$27.769^{+0.023}_{-0.022}$	Gaia
Other Stellar Parameters			
$v \sin i_*$	Stellar rotational velocity in km $\rm s^{-1}$	<2	This work
RV	Absolute radial velocity in km $\rm s^{-1}$ (γ)	-41.58 ± 0.26	This work
U	Galactic U velocity (km $\rm s^{-1}$)	-5.8 ± 0.2	This work
V	Galactic V velocity (km $\rm s^{-1}$)	-40.3 ± 0.4	This work
W	Galactic W velocity (km $\rm s^{-1}$)	-27.9 ± 0.6	This work

Notes. References: TIC (Stassun et al. 2018, 2019), Gaia (Gaia Collaboration 2018), APASS (Henden et al. 2015), 2MASS/WISE (Cutri et al. 2014), Bailer-Jones (Bailer-Jones et al. 2018).

[a] Derived using the HPF spectral matching algorithm from Stefansson et al. (2020a).

[b] `EXOFASTv2` derived values using MIST isochrones with the Gaia parallax and spectroscopic parameters in and using the spectral matching parameters derived from the HPF spectral matching analysis as priors.

the system orbiting at or close to orbital resonances with planets b or c. As such, TOI-1266 joins the ranks of other compact M dwarf multiplanet systems that do not show clear TTVs (e.g., the three-planet L98-59 system discussed in Kostov et al. 2019 or the LHS 1140 system discussed in Dittmann et al. 2017 and Ment et al. 2019).

Additionally, we looked for signs of nontransiting planets in the HPF RVs. Figure 5 shows generalized LS periodograms of the HPF RVs, along with a number of activity indicators measured from the HPF spectra, including the dLW, the chromatic index (CRX), and the line indices of the three Ca II IRT lines. To calculate the activity indicators, we follow the definition and procedures in the `SERVAL` pipeline (Zechmeister et al. 2018), and we note that their use of HPF spectra, including listing the exact wavelength ranges used to calculate the Ca II IRT indices, is further discussed in Stefansson et al. (2020b). We calculate the generalized LS periodograms using the `astropy.timeseries` package, and we calculate the

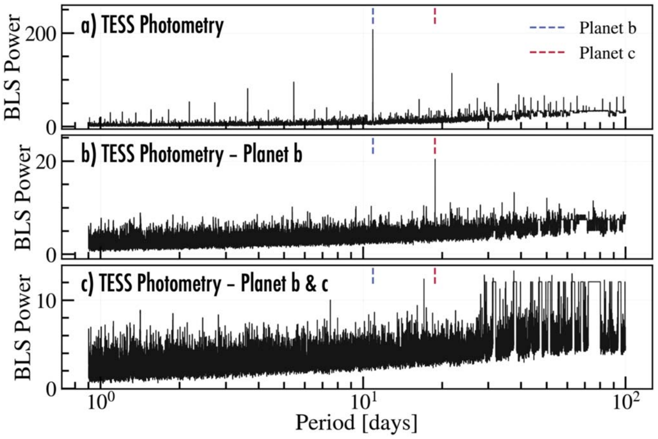

Figure 4. The BLS power spectra as a function of orbital period. (a) The BLS power spectrum of all available TESS photometry shows a clear peak at a period of $P = 10.89$ days (planet b; blue vertical line). (b) The BLS power spectrum of the TESS photometry after masking out transits of planet b shows a clear peak at $P = 18.80$ days (planet c; red vertical line). (c) The BLS power spectrum after masking out transits of planets b and c shows no further clear peaks.

false-alarm probabilities (FAPs)[27] using the `bootstrap` method implemented in the same package. In Figure 5, we additionally show the window function (WF) of our RV observations. All of the periodograms in Figure 5 are normalized using the formalism in Zechmeister & Kürster (2009), except the WF is normalized such that the highest peak has a power of 1. Table 4 in Appendix B lists the values of the RVs and activity indicators.

From Figure 5, we see no significant peaks (with FAP $< 0.1\%$), with no clear peaks seen at the known planet periods. We attribute the latter to the expected RV amplitude of the planets (3.3 and 1.6 $\mathrm{m\,s^{-1}}$ for planets b and c, respectively) being below the median HPF RV precision of 7.4 $\mathrm{m\,s^{-1}}$ (see Section 6.1). We note that we see a hint of two peaks at 1.779 days and its 1 day alias of 2.230 days in the RVs (Figure 5a), although both peaks have a low significance with an FAP $> 1\%$. Although there remains a possibility that there are other planets in the system that could contribute additional variability to the RVs, further data are required to confidently rule out or confirm their presence. In the absence of strong evidence for more planets in the system, we fit the available data sets (photometry and RVs) assuming the two known transiting planets in the system.

4.2. Transit, RV, and Gaussian Process Modeling

We jointly model the available photometry from TESS and the two ground-based transits along with the radial velocities using the `juliet` code (Espinoza et al. 2019). In `juliet`, we used the `dynesty` package (Speagle 2020) to perform dynamic nested sampling for parameter estimation. The `juliet` code uses the `batman` package (Kreidberg 2015) for the transit model—which uses the transit prescription from Mandel & Agol (2002)—and the `radvel` package (Fulton et al. 2018) for the RV model. Following the implementation in `juliet`, we parameterize the transit in terms of the radius ratio ($p = R_p/R_*$) and the impact parameter b. As we are using the TESS PDCSAP flux, which already corrects for dilution in the TESS aperture—which in this case is minimal due to the lack of nearby bright targets—we fix the dilution factor D in `juliet` for the TESS and ground-based photometry to $D = 0$. As both the ground-based and TESS transits were observed in similar bandpasses (TESS bandpass and SDSS r' and i' filters), we assume that the transit depths in the TESS and ground-based transits are identical. We use a quadratic limb-darkening law to describe the transits, where we elect to use the q_1 and q_2 limb-darkening parameterization from Kipping (2013), and to minimize biases in the resulting planet parameter constraints, we follow the suggestion in Espinoza & Jordán (2015) and place uniform priors on the limb-darkening parameters from zero to 1.

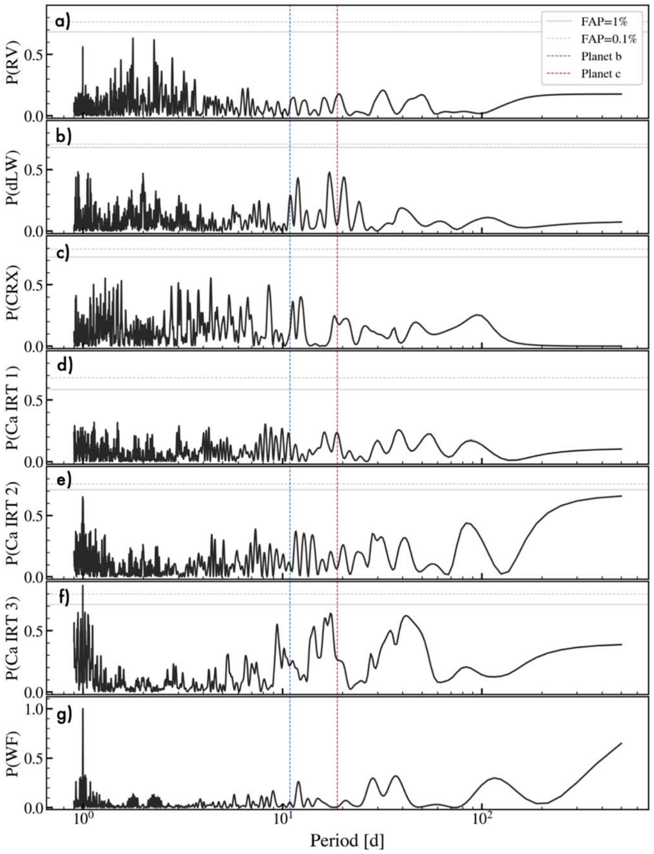

Figure 5. The LS periodograms of the HPF RVs along with different activity indicators. The periods of planets b and c are highlighted with the dashed blue and red lines, respectively. The FAPs of 1% and 0.1% calculated using the bootstrap method are denoted with the gray solid and dashed lines, respectively. (a) HPF RVs; (b) dLW activity indicator; (c) CRX activity indicator; (d)–(f) Ca II IRT indices for the three Ca II IRT lines; (g) WF of the HPF RVs showing a clear sampling peak at 1 day. The power in panels (a)–(f) is normalized using the formalism in Zechmeister & Kürster (2009), and panel (g) is normalized so that the highest peak is unity.

To check if both transits recovered consistent stellar densities, we first performed a fit assuming circular orbits for both planets without an explicit prior on the stellar density. In doing so, we recover a stellar density of $\rho_* = 9.2 \pm 1.4$ and $7.0^{+5.0}_{-3.9}$ g cm^{-3} from the transits of planets b and c, respectively. From this, we see that both values are consistent with the model-dependent stellar density from Table 1 of $\rho_* = 8.13 \pm 0.48$ g cm^{-3}, suggesting that the two planets indeed transit TOI-1266. This consistency between the transit-derived stellar density assuming circular orbits and the model-dependent stellar density further

---

[27] Although the FAP is commonly used in periodogram analysis in radial velocity data, it has known limitations (see, e.g., discussion in Fischer et al. 2016).

Table 2
Summary of Priors Used for Our Joint Transit and RV Fit

Parameter	Description	Model
Orbital Parameters—Planet b		
P	Orbital period (days)	$\mathcal{U}(10.89, 10.91)$
T_C	Transit midpoint—2,458,000 ($\mathrm{BJD_{TDB}}$)	$\mathcal{U}(690.95, 691.05)$
R_p/R_*	Scaled radius	$\mathcal{U}(0, 1)$
a/R_*	Scaled semimajor axis	$\mathcal{U}(1, 100)$
b	Impact parameter	$\mathcal{U}(0, 1)$
K	RV semi-amplitude (m s^{-1})	$\mathcal{U}(0, 100)$
Orbital Parameters—Planet c		
P	Orbital period (days)	$\mathcal{U}(18.79, 18.81)$
T_C	Transit midpoint—2,458,000 ($\mathrm{BJD_{TDB}}$)	$\mathcal{U}(689.90, 690.00)$
R_p/R_*	Scaled radius	$\mathcal{U}(0, 1)$
a/R_*	Scaled semimajor axis	$\mathcal{U}(1, 100)$
b	Impact parameter	$\mathcal{U}(0, 1)$
K	RV semi-amplitude (m s^{-1})	$\mathcal{U}(0, 100)$
Other Constraints		
ρ_*	Stellar density (g cm^{-3})	$\mathcal{N}(8.13, 0.48)$
Instrumental Terms		
q_1[a]	Limb-darkening parameter	$\mathcal{U}(0, 1)$
q_2[a]	Limb-darkening parameter	$\mathcal{U}(0, 1)$
σ_{phot}[b]	Photometric jitter (ppm)	$\mathcal{J}(1, 5000)$
μ_{phot}[b]	Photometric baseline	$\mathcal{N}(0, 0.1)$
σ_{HPF}	HPF RV jitter (m s^{-1})	$\mathcal{J}(0.01, 100)$
γ	HPF RV offset (m s^{-1})	$\mathcal{U}(-50, 50)$
TESS Quasiperiodic GP Parameters		
P_{GP}	GP period (days)	$\mathcal{J}(0.1, 1000)$
B	GP amplitude (ppm^2)	$\mathcal{J}(10^{-6}, 1)$
C	GP additive factor	$\mathcal{J}(10^{-3}, 10^{3})$
L	GP length scale (days)	$\mathcal{J}(1, 10^{3})$
Perkin 0.4 m Approximate Matern 3/2 GP Parameters		
σ_{GP}	GP amplitude (ppm)	$\mathcal{J}(0.1, 10^{4})$
L	Timescale of exp. kernel (days)	$\mathcal{J}(0.01, 10^{5})$
ρ	Timescale of Matern kernel (days)	$\mathcal{J}(0.01, 10^{5})$
APO 3.5 m Approximate Matern 3/2 GP Parameters		
σ_{GP}	GP amplitude (ppm)	$\mathcal{J}(0.1, 10^{4})$
L	Timescale of exp. kernel (days)	$\mathcal{J}(0.01, 10^{5})$
ρ	Timescale of Matern kernel (days)	$\mathcal{J}(0.01, 10^{5})$

Notes. Here $\mathcal{N}(\mu, \sigma)$ denotes a normal prior with mean μ and standard deviation σ; $\mathcal{U}(a, b)$ denotes a uniform prior with a start value a and end value b; and $\mathcal{J}(a, b)$ denotes a Jeffreys prior truncated between a start value a and end value b. We assumed circular orbits for both planets.

[a] We use the same uniform priors for pairs of limb-darkening parameters q_1 and q_2 (parameterization from Kipping 2013) and separate limb-darkening parameters for each instrument).

[b] For each photometric data set (TESS, 0.4 m Perkin, and 3.5 m APO), we placed a separate photometric jitter and baseline offset term.

suggests that both planets have low eccentricities, which conforms with the trend that multitransiting systems generally show low eccentricities (Van Eylen & Albrecht 2015). As such, without strong evidence suggesting noncircular orbits, for our final parameter estimation, we assumed that both planets have circular orbits. We further place a Gaussian prior on the stellar density of $\rho_* = 8.13 \pm 0.48\,\mathrm{g\,cm^{-3}}$ to accurately constrain the orbital distance (a/R_*) of both planets. In total, we fit for 36 parameters. Table 2 summarizes the priors we used.

To account for correlated noise in the photometric data sets, we use a Gaussian process noise model, where we choose different kernels for the different data sets to best reflect the characteristic noise structures seen in the data as a function of time. For the TESS data, to account for any possible low-level photometric modulations, we use the quasiperiodic kernel from the `celerite` package (Foreman-Mackey et al. 2017)[28] with hyperparameters B, C, L, and P_{rot}: B and C tune the weight of the exponential decay component of the kernel with a decay constant of L (in days), and P_{GP} corresponds to the periodicity of the quasiperiodic oscillations, which we interpret as the stellar rotation period.

For the ground-based data sets, we follow Stefansson et al. (2020b) and use the approximate Matern 3/2 kernel multiplied by an exponential kernel available in `juliet`.[29] This kernel has covariance properties that are better matched to shorter-term instrumental and/or atmospheric red-noise structures often seen in ground-based data sets (see, e.g., Pepper et al. 2017; Espinoza et al. 2019). This kernel has the hyperparameters σ_{GP}, which denotes the photometric amplitude in ppm; L, which is the length scale of the exponential component in days; and ρ, which is the length scale of the Matern 3/2 kernel in days.

For the RV data set, given the few RV points available and the low activity of the star, we do not use a Gaussian process model but rather adopt a white-noise model to account for potential systematics and/or stellar jitter effects.

4.3. Derived Planet Parameters

Figure 2 shows the TESS and ground-based transits, along with our best-fit model. Figure 6 shows the RVs from HPF, showing the unbinned RVs as a function of time, as well as the RVs phased around each planet. Table 3 shows the resulting planet parameters from our joint fit of the photometry and the radial velocities. To cross-check the parameters reported by `juliet`, which uses nested sampling, we performed a separate fit using the `exoplanet` code (Foreman-Mackey et al. 2020), which uses the `PyMC3` Markov Chain Monte Carlo package for parameter estimation (Salvatier et al. 2016). The `exoplanet` package builds on the `theano` package (Theano Development Team 2016) for the numerical infrastructure and uses the `starry` package (Luger et al. 2019) for light-curve generation. This test resulted in parameters fully consistent (within 1σ) with the parameters reported by `juliet`. For brevity, we adapt the parameters from `juliet` in Table 3.

5. Statistical Validation

To estimate the probability that the transits we observed were due to astrophysical false positives, we used the statistical techniques of Morton (2012) implemented in the Validation of Exoplanet Signals using a Probabilistic Algorithm (`VESPA`) package (Morton 2015). `VESPA` calculates the false-positive probability (FPP) of transiting planet candidates by simulating and determining the likelihood of a range of astrophysical false-positive scenarios that could replicate the observed light curves, including background eclipsing binaries, eclipsing binaries, and hierarchical eclipsing binaries. As inputs to `VESPA`, we used (a) the phase-folded TESS transit in a 2× transit duration window around the center of each transit; (b) the position of the target in the sky; (c) the Two Micron All Sky Survey (2MASS) J, H, K, SDSS g', r', i', and TESS

---

[28] See Equation (56) in Foreman-Mackey et al. (2017) for the functional form of the kernel.

[29] See Section 2.3 in Espinoza et al. (2019) for the functional form of the kernel.

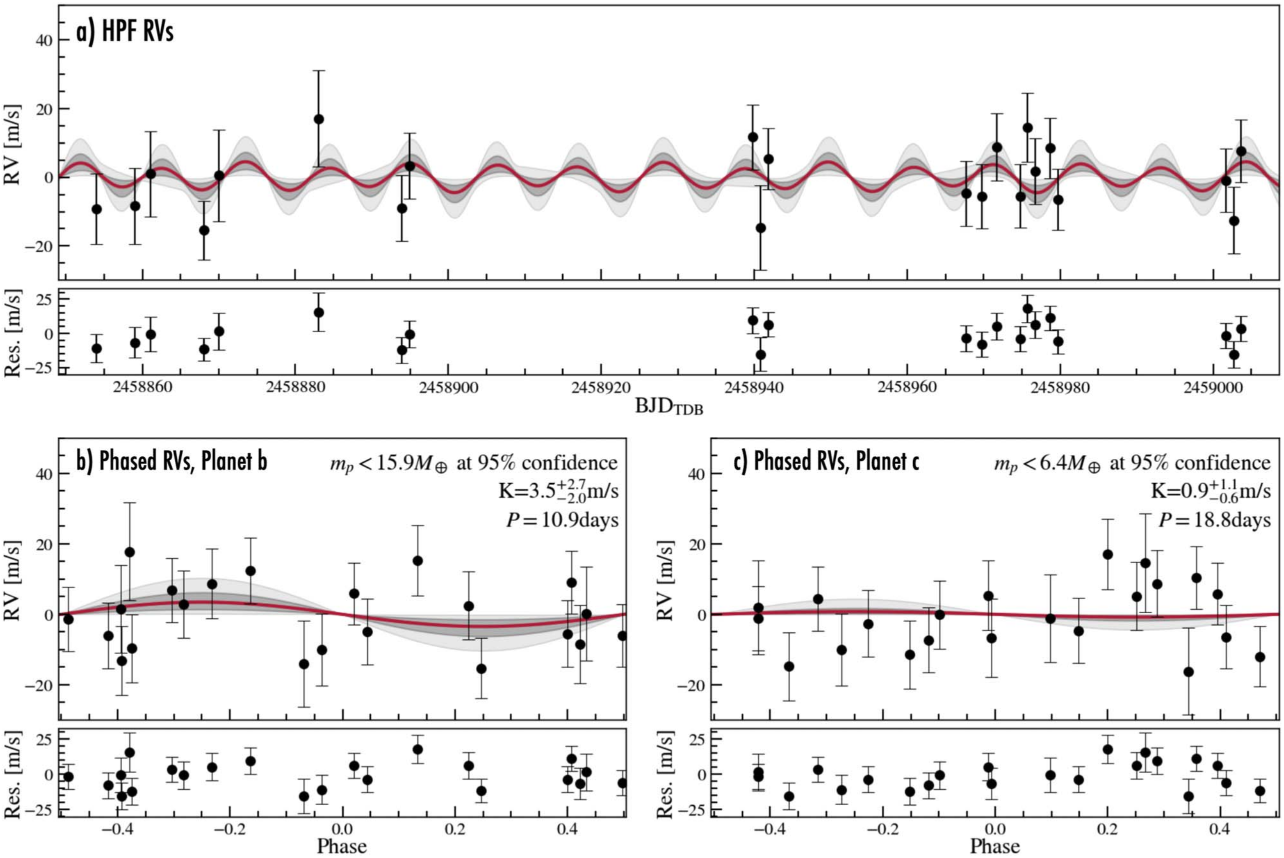

Figure 6. The RVs from HPF as a function of time (panel (a)), and panels (b) and (c) show the RVs folded on the periods of planets b and c, respectively. The median best-fit model is shown in red. The gray shaded regions show the 68% and 99.7% credible intervals from the posteriors.

magnitudes; (d) the Gaia parallax; (e) the host star stellar effective temperature, surface gravity, and metallicity; and (f) the maximum visual extinction from estimates of Galactic dust extinction (Green et al. 2019). These values are listed in Table 1.

In addition to the inputs above, `VESPA` requires two additional constraints. First, as we have ground-based transit observations of both planets recovering fully consistent transits with the TESS transits but at a finer pixel scale, we set the maximum separation for a background eclipsing object equal to the aperture radius used for the ground-based photometric extractions for planets b (7″ from Perkin) and c (8″ from APO), respectively. Second, we set the maximum depth of the secondary eclipse equal to the rms of the unbinned TESS light curve (2262 ppm). Assuming the more conservative approach that the transits of planets b and c are independent, we obtain FPP rates of 8×10^{-6} and 1.9×10^{-3} for planets b and c, respectively. Although already showing low FPP values, we argue that the real FPPs are even lower, accounting for false-positive scenarios being less likely in multiplanet systems (e.g., Latham et al. 2011; Lissauer et al. 2012). We consider both planets statistically validated.

6. Discussion

6.1. Mass and Bulk Composition Constraints

From the HPF RVs, we obtain formal mass constraints of $6.9^{+5.5}_{-4.0}$ and $1.9^{+2.3}_{-1.3} M_\oplus$ for planets b and c, respectively, which we use to place upper mass constraints of 15.9 and 6.4 $M_\oplus$ at 95% confidence (2σ) for the two planets, respectively. The corresponding 99.7% constraints are 22.3 and 11.3 $M_\oplus$, respectively. We compared these mass constraints with the predicted masses calculated with the mass–radius relations in the `Forecaster` (Chen & Kipping 2017) and `MRExo` (Kanodia et al. 2019) mass–radius packages. `Forecaster` uses a broken power-law mass–radius relation to predict exoplanet masses from their radii derived from a sample of exoplanets across different spectral types, while the `MRExo` package uses a nonparametric relation specifically trained on current M dwarf planet systems with well-measured masses and radii (Kanodia et al. 2019). From `Forecaster`, we predict masses of $6.6^{+5.0}_{-2.8}$ and $3.8^{+2.6}_{-1.4} M_\oplus$ for planets b and c, translating to expected RV semi-amplitudes of $3.3^{+2.5}_{-1.4}$ and $1.6^{+1.0}_{-0.6}$ m s^{-1}, respectively. From `MRExo`, we predict masses of $6.2^{+6.7}_{-3.2}$ and $2.9^{+5.1}_{-1.7} M_\oplus$ for planets b and c, respectively. We see that our current mass constraints are fully consistent with the predicted mass estimates.

Using our formal mass constraints, in Figure 7, we explore the most likely composition of the two planets by comparing our posteriors to the composition models of Zeng et al. (2019). From Figure 7, we can see that both planets are consistent with nonrocky compositions favoring either a water-rich world (e.g., the 100% H_2O model) and/or a rocky core enveloped by an H/He atmosphere.[30] For planet b, if we assume the two-component

---

[30] In general, from exoplanet masses and radii alone, we cannot discern between such solutions, as there are degeneracies in the composition models of small planets (see, e.g., Adams et al. 2008; Zeng et al. 2019).

Table 3
Median Values and 68% Credible Intervals from Our Joint Fit of the Photometry and Radial Velocity Data of TOI-1266

Parameter	Description	Planet b		Planet c
T_C (BJD$_{\rm TDB}$)	Transit midpoint	$2,458,691.005^{+0.001,1}_{-0.001,1}$		$2,458,689.958,9^{+0.006,0}_{-0.005,0}$
P (days)	Orbital period	$10.894,879^{+0.000,07}_{-0.000,07}$		$18.801,52^{+0.000,54}_{-0.000,67}$
R_p/R_*	Radius ratio	$0.053,2^{+0.001,5}_{-0.001,2}$		$0.036,3^{+0.001,7}_{-0.002,2}$
R_p ($R_\oplus$)	Planet radius (Earth radii)	$2.458^{+0.083}_{-0.073}$		$1.673^{+0.087}_{-0.110}$
R_p ($R_{\rm J}$)	Planet radius (Jupiter radii)	$0.219,3^{+0.007,4}_{-0.006,6}$		$0.149,2^{+0.007,7}_{-0.009,5}$
$\delta_{p,{\rm K2}}$	Transit depth	$0.002,83^{+0.000,16}_{-0.000,13}$		$0.001,32^{+0.000,13}_{-0.000,16}$
a/R_*	Normalized orbital radius	$37.9^{+2.2}_{-3.5}$		$52.66^{+0.97}_{-0.73}$
a (AU)	Semimajor axis (from a/R_* and R_*)	$0.074,5^{+0.004,6}_{-0.006,9}$		$0.103,7^{+0.002,6}_{-0.002,5}$
$\rho_{*,{\rm transit}}$ (g cm^{-3})	Density of star	$8.7^{+1.6}_{-2.2}$		$7.81^{+0.44}_{-0.32}$
i (deg)	Transit inclination	$89.36^{+0.20}_{-0.33}$		$89.225^{+0.060}_{-0.043}$
b	Impact parameter	$0.43^{+0.16}_{-0.12}$		$0.714^{+0.035}_{-0.050}$
e	Eccentricity		0 (adopted)	
ω (deg)	Argument of periastron		90 (adopted)	
$T_{\rm eq}$ (K)	Equilibrium temp. (assuming $a = 0.0$)	$410.0^{+21.0}_{-15.0}$		$347.1^{+7.9}_{-8.0}$
$T_{\rm eq}$ (K)	Equilibrium temp. (assuming $a = 0.3$)	$287.0^{+15.0}_{-11.0}$		$243.0^{+5.6}_{-5.6}$
S ($S_\oplus$)	Insolation flux	$4.72^{+1.0}_{-0.66}$		$2.42^{+0.23}_{-0.22}$
T_{14} (days)	Transit duration	$0.087,9^{+0.001,7}_{-0.001,6}$		$0.085,3^{+0.004,6}_{-0.003,6}$
T_{23} (days)	Transit duration	$0.076,7^{+0.001,9}_{-0.002,1}$		$0.073,5^{+0.005,6}_{-0.004,5}$
τ (days)	Ingress/egress duration	$0.005,37^{+0.001,4}_{-0.000,60}$		$0.005,89^{+0.000,53}_{-0.000,64}$
K (m s^{-1})	RV semi-amplitude	$3.5^{+2.7}_{-2.0}$		$0.8^{+0.97}_{-0.53}$
m_p ($M_\oplus$)	Planet mass	<15.9 at 95% confidence		<6.4 at 95% confidence
$\sigma_{\rm w,HPF}$ (m s^{-1})	HPF RV jitter		$6.5^{+2.0}_{-1.6}$	
γ (m s^{-1})	HPF RV offset		$0.3^{+1.8}_{-1.9}$	

Note. Both planets are assumed to be on circular orbits. The formal 68% credible intervals for the masses of the two planets are $6.9^{+5.5}_{-4.0}$ and $1.9^{+2.3}_{-1.3} M_\oplus$ for planets b and c, which we use to place 95% upper limits on the mass, as listed below.

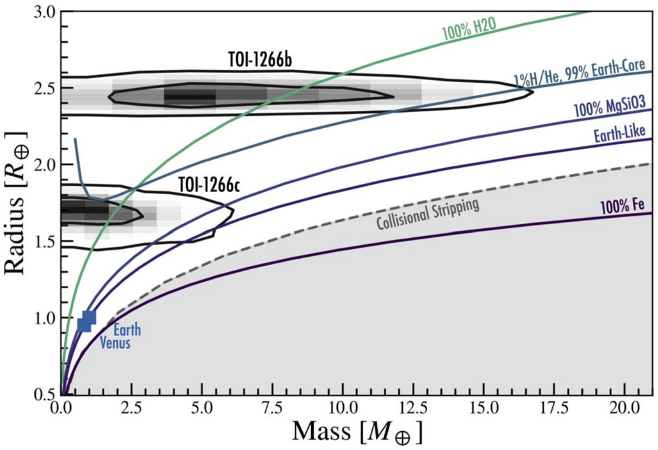

Figure 7. Current radius and mass constraints of TOI-1266b and c from our joint two-planet fit. The contours show our 1σ and 2σ posterior contours for planets b and c. The shaded gray region indicates planets with iron content exceeding the maximum value predicted from models of collisional stripping (Marcus et al. 2010). The solid lines show different composition models from Zeng et al. (2019). Earth and Venus are denoted by blue squares. Further RV observations are needed to more precisely constrain the masses of both planets.

model of Lopez & Fortney (2014) consisting of a rocky core enveloped by a predominantly H/He atmosphere, we estimate a gas composition mass fraction of 1.5%–2.0%. For planet c, although our RVs currently only show a marginal nonzero detection of the low-RV amplitude signal, our current RV constraints suggesting a mass $<6.4\ M_\oplus$ at 95% confidence hint at a non-Earth-like composition, tilting toward a water-rich or rocky world enshrouded by an H/He atmosphere. Further RVs are required to confirm and better constrain the composition of both planets, in particular planet c. As TOI-1266 is a relatively nearby and bright ($V = 12.9$, $J = 9.7$) early M dwarf, an accurate mass measurement of both planets is within reach of current high-precision spectrographs. To estimate the number of additional visits needed to measure the masses for transiting planets with known periods, we used the methodology of Plavchan et al. (2015). Assuming the RV semi-amplitudes expected from `Forecaster`, we estimate that we would need 10–20 more HPF visits to measure the mass of planet b at 99.7% confidence (3σ), but measuring the mass of planet c is currently infeasible in <100 visits with HPF. However, as TOI-1266 is a relatively bright early M dwarf, the RV information content is better matched for red-optical Doppler spectrographs such as NEID (Schwab et al. 2016), CARMENES (Quirrenbach et al. 2018), ESPRESSO (Pepe 2018), KPF (Gibson et al. 2016), or MAROON-X (Seifahrt et al. 2016). With NEID, assuming a 2.8 m s^{-1} RV precision in 30 minute bins, we estimate being able to measure the masses of planets b and c in ~six and ~30 visits at 3σ, respectively.

6.2. TOI-1266c Resides in the Radius Valley

Close-in exoplanets display a gap or valley in the radius distribution around 1.5–2.0 $R_\oplus$ (Owen & Wu 2013; Fulton et al. 2017; Van Eylen et al. 2018; Cloutier & Menou 2020), which has been interpreted as the transition radius between rocky and gaseous planets. A number of theoretical models have arisen to explain the emergence of the radius valley that predict that the location of the rocky-to-gaseous transition radius, $r_{\rm transition}$, depends on the orbital period of the planet.

First, the photoevaporation model, where the atmosphere of small planets can be stripped by high-energy XUV photons leaving behind bare planetary cores (Lopez et al. 2012; Owen & Wu 2013; Lopez & Fortney 2013; Owen & Wu 2017; Lopez & Rice 2018), predicts that the transition radius should decrease with orbital period as $r_{\rm transition} \propto P^{-0.15}$. Second, the core-powered mass-loss mechanism (Ginzburg et al. 2016, 2018; Gupta & Schlichting 2019), where the luminosity of the cooling planetary core provides the energy for atmospheric loss, predicts that the transition radius should also decrease with orbital period as $r_{\rm transition} \propto P^{-0.13}$. Third, atmospheric erosion via giant impacts predicts that the transition radius should decrease more steeply with orbital period as $r_{\rm transition} \propto P^{-0.33}$ (Inamdar & Schlichting 2015; Liu et al. 2015; Wyatt et al. 2020). Lastly, in the gas-poor formation scenario, where super-Earths represent a distinct population of planets forming in a gas-poor environment after the protoplanetary disk has dissipated (Lee et al. 2014; Lee & Chiang 2016; Lopez & Rice 2018), the prediction is instead that the transition radius should increase with orbital period as $r_{\rm transition} \propto P^{0.11}$.

To distinguish between these scenarios, previous studies have empirically measured the location of the radius valley as a function of orbital period. Martinez et al. (2019) used data from Kepler and the California Kepler Survey (CKS) to show that the location of the radius valley decreases as $r_{\rm transition,M19} \propto P^{-0.11 \pm 0.03}$ around solar-type stars, consistent with mechanisms of photoevaporation and core-powered mass loss but inconsistent with the giant impact erosion and gas-poor formation mechanisms. This is in good agreement with the dependence of $r_{\rm transition,VE18} \propto P^{-0.09^{+0.02}_{-0.04}}$ measured by Van Eylen et al. (2018) using a sample of planets orbiting solar-type stars with accurately determined stellar parameters from asteroseismology. Recently, Cloutier & Menou (2020) constrained the location of the radius valley for later-type stars (mid-K to mid-M; $T_{\rm eff} < 4700$ K) using data from Kepler and K2, obtaining $r_{\rm transition,CM20} \propto P^{0.058 \pm 0.022}$. Their measurement has a power-law slope with the opposite sign to the power-law slope measured by Martinez et al. (2019) around Sun-like stars and is more consistent with models predicting that small planets represent a population of planets that form late in a gas-poor environment (Lee et al. 2014; Lee & Chiang 2016; Lopez & Rice 2018). Cloutier & Menou (2020) interpret this as either planet formation being governed by a separate process around M dwarfs (i.e., gas-poor formation) or the efficiency of atmospheric postprocessing (such as photoevaporation) being weakened for planets orbiting low-mass stars.

In Figure 8, we show planet radius as a function of orbital period for small ($R < 4$ $R_\oplus$) M dwarf planets with mass measurements better than 50%,[31] which we compare to the radius valley locations as measured by Martinez et al. (2019) around Sun-like stars and Cloutier & Menou (2020) for M dwarfs. Following Cloutier & Menou (2020), in Figure 8, we plot the radius valley location of Martinez et al. (2019) after scaling to the M dwarf mass regime. Specifically, we plot the radius valley location in r–P space, as given by Equations (10) and (11) in Cloutier & Menou (2020), as

$$r_{\rm transition,M19} = -0.48 \log_{10}(P) + 2.32 \tag{1}$$

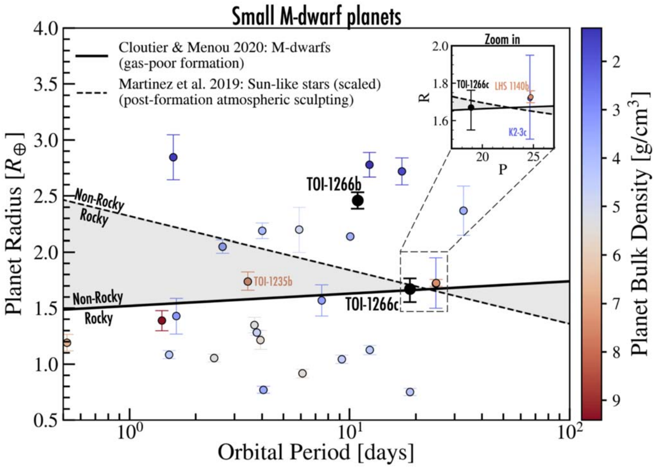

Figure 8. Planet radius for small M dwarf planets ($R < 4$ $R_\oplus$) as a function of orbital period. Black points show TOI-1266b and c. Planets with better than 50% mass constraints have their bulk density highlighted with the color gradient. The solid black line shows the location of the rocky-to-gaseous transition radius $r_{\rm transition}$ for planet host stars with $T_{\rm eff} < 4700$ K as measured by Cloutier & Menou (2020), consistent with the predictions of gas-poor formation. The dashed line shows $r_{\rm transition}$ as a function of orbital period as measured by Martinez et al. (2019) around solar-type stars (scaled to the low-mass regime), consistent with the predictions of photoevaporation or core-powered mass-loss models. Planet c lies in the transition region, as predicted by Cloutier & Menou (2020) and Martinez et al. (2019), and could thus have either a predominantly rocky or nonrocky composition. The inset highlights the position of TOI-1266c and two other M dwarf planets also residing in the radius valley: K2-3c and LHS 1140b, which are observed to be gaseous and rocky, respectively. The data were obtained from the NASA Exoplanet Archive on 2020 May 20 (Akeson et al. 2013).

for solar-type stars and

$$r_{\rm transition,CM20} = 0.11 \log_{10}(P) + 1.52 \tag{2}$$

for M dwarf stars.

From Figure 8, with a period of $P = 18.8$ days and radius of 1.67 $R_\oplus$, we see that TOI-1266c lands in the transition region, as predicted by Cloutier & Menou (2020) for late K and M dwarf systems (Equation (2)) and Martinez et al. (2019) for Sun-like stars (Equation (1)). As such, TOI-1266c could have a rocky or predominantly nonrocky composition (e.g., a water-rich world or retaining a few percent H/He atmosphere). The inset in Figure 8 further highlights the position of TOI-1266c and two other M dwarf planets also residing in the transition region: K2-3c and LHS 1140b, which interestingly show different bulk compositions. Here K2-3c has a radius of 1.72 ± 0.22 $R_\oplus$ (Crossfield et al. 2015) and a mass of 2.1 ± 1.0 $M_\oplus$ (Kosiarek et al. 2019); thus, it has a bulk density of $\rho \sim 3$ g cm^{-3}, suggestive of a nonrocky composition. However, LHS 1140b (Dittmann et al. 2017; Ment et al. 2019) has a radius of 1.727 ± 0.032 $R_\oplus$, mass of 7.0 ± 0.9 $M_\oplus$, and bulk density of $\rho \sim 7.5$ g cm^{-3}, consistent with a rocky composition.

From Figure 8, we also note that both LHS 1140b and TOI-1235b—a planet recently discovered and characterized by Cloutier et al. (2020) and Bluhm et al. (2020)—have densities consistent with rocky compositions, but both reside above the line measured by Cloutier & Menou (2020), where we would have predicted them to have a nonrocky composition. This could suggest that the transition region could lie slightly higher than measured in Cloutier & Menou (2020). Another explanation would be that the efficiency of different processes

---

[31] We note here that imposing a mass constraint introduces an observational bias, as lower-mass planets are less likely to have good fractional mass precision.

sculpting planetary compositions varies for planets in the transition region, resulting in a continuum of possible compositions. This would be compatible with the trend noted by Fulton & Petigura (2018) and Cloutier & Menou (2020) that the radius valley is not completely void of planets and gets increasingly filled with decreasing stellar masses. As mentioned by Cloutier & Menou (2020), this trend has not been firmly tested yet. A precise mass constraint of TOI-1266c, along with other planets residing in the radius valley, can directly help place further constraints on this trend.

6.3. *TOI-1266c: A Planet in the Venus Zone*

With a radius of $R = 1.67\ R_{\oplus}$ and an incident stellar flux 2.4 times that of Earth, if TOI-1266c has a rocky composition, it could potentially be a "super-Venus" (see, e.g., Kane et al. 2013 and Kane et al. 2014 for a discussion of "super-Venuses"). Venus itself receives 1.91 times more flux than Earth and is 95% the size of Earth. Kane et al. (2014) defined "super-Venuses" as predominantly rocky planets residing in the "Venus zone," where planets receive insolation fluxes between ~0.95 and 25 times that of Earth.[32] Future studies attempting to identify atmospheric abundances of small rocky planets will face the challenge of distinguishing between possible Venus and Earth surface conditions (Kane et al. 2014). There is a need to discover more planets that may have evolved into a postrunaway greenhouse state so that we can target their atmospheres for characterization with future facilities such as the James Webb Space Telescope.

As discussed in Section 6.1 and Figure 7, it is also possible that TOI-1266c could have retained an H/He atmosphere and/or have a higher water fraction than Earth. If TOI-1266c is determined to be a water-rich world, it remains to be seen how much of it is retained due to the high-luminosity pre-main-sequence evolution of its M dwarf host star (Luger & Barnes 2015) and any historical stellar activity. We note that TOI-1266c lies firmly on the side of the "cosmic shoreline" where the gravitational binding of the atmosphere to the planet is high compared to the insolation-driven escape (see Figure 1 in Zahnle & Catling 2017), hinting that TOI-1266c could retain a water atmosphere. Interestingly, TOI-1266c also lies very close to or on top of the "H_2O greenhouse runaway" region in Zahnle & Catling (2017). Depending on the age of the system, stellar UV activity, and initial water content accumulated at the early stages of the system evolution, and considering the insolation on the planet, TOI-1266c could host a hot/moist water vapor atmosphere. Such an atmosphere has recently been detected around the mini-Neptune K2-18b (Benneke et al. 2019; Tsiaras et al. 2019). Further detecting such atmospheres would provide a valuable data point in capturing systems that are undergoing moist or runaway greenhouse climates and provide clues to atmospheric evolutionary history similar to that of the evolution of our own terrestrial planets in the solar system. It would also have implications for initial volatile compound inventories for models of planet formation.

We estimated the applicability of performing transmission spectroscopy on both planets using the transmission spectroscopy metric (TSM) as defined in Kempton et al. (2018). We obtain a fairly large spread of possible TSMs of 53^{+51}_{-19} for planet b using our current mass constraint. Although the median value of 53 is formally below the TSM > 90 prioritization threshold for mini-Neptune planets with radii larger than 1.5 $R_{\oplus}$ recommended by Kempton et al. (2018), a further precise mass constraint is needed to discern the exact value of the TSM. For planet c, the TSM will depend strongly on whether the planet has retained an H/He atmosphere or is predominantly rocky with a minimal atmosphere. In their definition of the TSM, Kempton et al. (2018) defined the transition between predominantly rocky planets and gaseous mini-Neptunes at 1.5 $R_{\oplus}$. If we assume TOI-1266c to be a characteristic mini-Neptune, we obtain a TSM of 30^{+19}_{-15}; if we assume it to be rocky, we obtain a TSM of 5^{+3}_{-2}. As such, the favorability of TOI-1266c for atmospheric characterization depends strongly on whether it is determined to be predominantly rocky or nonrocky.

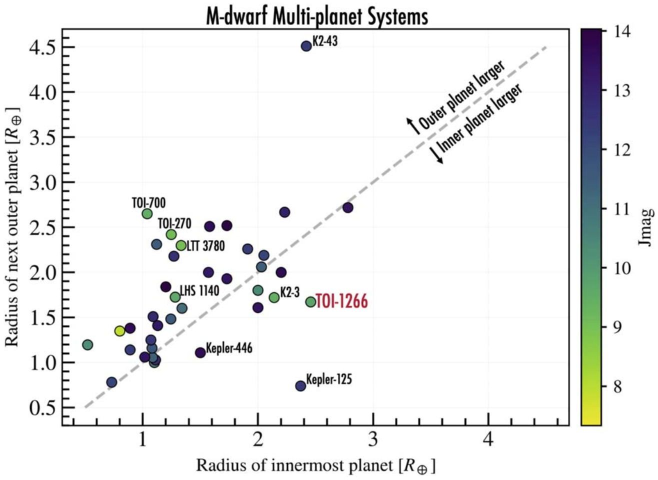

Figure 9. Radii of planets orbiting in M dwarf multiplanet systems showing the radius of the outer planet vs. the radius of the innermost planet. The star TOI-1266 is one of the few such systems where the innermost planet is substantially larger than the next outer planet. For simplicity, for systems with more than two transiting planets, we only show the innermost two most highly irradiated planets.

6.4. *Inverted Planet Radii: Planet b is Larger than Planet c*

The star TOI-1266 represents one of the few M dwarf systems with close-in planets where the innermost planet is substantially larger than the next outer planet. Figure 9 compares the radii of inner planets to outer planets in multiplanet M dwarf systems.[33] From Figure 9, we see that Kepler-125 represents such a case: it has two known planets, where the innermost planet has a radius of 2.37 $R_{\oplus}$, and the substantially smaller next outer planet has a radius of 0.74 $R_{\oplus}$ (Rowe et al. 2014). Additionally, from Figure 9, we see that TOI-1266 is similar to the K2-3 system in terms of both orbital periods and planetary radii; this system has three planets with orbital periods of 10.1, 24.6, and 44.6 days and radii of 2.14, 1.72, and 1.52 $R_{\oplus}$, respectively, where interestingly, the innermost planet is the largest in the system (Crossfield et al. 2015). Kosiarek et al. (2019) measured the masses of the two innermost K2-3 planets, measuring masses of 6.5 and 2.14 $M_{\oplus}$, while the mass of the outermost planet d was not significantly detected ($<2.80\ M_{\oplus}$ at 3σ). This results in a fairly low density

---

[32] The exact bounding values of the Venus zone are dependent on the effective temperature of the host star; see Figure 3 in Kane et al. (2014). We have focused here on the bounding values Kane et al. (2014) reported for M dwarf systems.

[33] Data taken from the NASA Exoplanet Archive (Akeson et al. 2013) in 2020 August.

for planet c with $\rho_c = 2.98\,\mathrm{g\,cm^{-3}}$, which could mean that it has a water-rich composition. Due to the striking similarities of both systems, it will be interesting to see if TOI-1266c is also observed to have a low density. The brightness of TOI-1266 makes the system amenable for precision RV observations to constrain the masses of the planets, gaining further insights into the composition of systems where the innermost planet is larger than the next outer planet.

In comparing the radii of planet pairs in a sample of multiplanet systems from Kepler, Weiss et al. (2018) found that outer planets tend to be larger than inner planets in ∼65% of cases in their sample. As mentioned by Weiss et al. (2018), this could be explained by atmospheric erosion from photoevaporation. Photoevaporation is more efficient at stripping the atmospheres of planets orbiting closer to their host stars, preferentially resulting in increasing radii with increasing orbital distances. However, the degree to which an atmosphere can be stripped via photoevaporation also depends on the mass of the planet.

Recently, Owen & Campos Estrada (2020) used multiplanet systems with planets that straddle the radius gap to test whether such systems were consistent with the predictions of the photoevaporation model. In their framework, Owen & Campos Estrada (2020) assumed that planets in a given multiplanet system form with rocky Earth-like cores and gaseous H/He envelopes that get eroded away with time via photoevaporation. To obtain a constraint on the minimum possible mass of the larger gaseous planet to be consistent with photoevaporation, they assumed that the planet below the radius gap had just barely had its atmosphere stripped due to photoevaporation. In an application of their model of 73 Kepler multiplanet systems, they found that 71 of the systems are consistent with this model, with two systems being inconsistent. The two inconsistent systems—Kepler-100 and Kepler 142—have striking similarities: they both are three-planet systems composed of two super-Earths (below the radius valley) and a mini-Neptune (above the radius valley), where the mini-Neptune is the middle planet. Although formally inconsistent using the original assumptions of the model, Owen & Campos Estrada (2020) mentioned that the two systems can be brought into agreement with the predictions of photoevaporation if some of the assumptions are changed. One possible scenario would be if the relative core compositions of the planets are changed, with the core density of the outer super-Earth being lowered by increasing the core fraction of ices/water, but such dissimilar core densities are proposed in some formation scenarios (Raymond et al. 2018).

With an inner mini-Neptune that is larger than the outer super-Earth, TOI-1266 is similar to the inconsistent systems studied by Owen & Campos Estrada (2020). To use the framework of Owen & Campos Estrada (2020)—which assumes two planets that straddle the radius valley—we would need to assume that TOI-1266c lies below the radius valley and has just gotten its atmosphere stripped away. Under this assumption, the model of Owen & Campos Estrada (2020) shows no valid solution for the system, suggesting that TOI-1266 would join the ranks of the "inconsistent systems" studied by Owen & Campos Estrada (2020). To bring TOI-1266 into agreement with the predictions of photoevaporation, some of the original assumptions of the Owen & Campos Estrada (2020) model could be changed, including assuming that planet c had a higher fraction of water/ices in its core. However, as it is still unclear whether TOI-1266c lies above or below the radius valley (see discussion in Section 6.2), the possibility remains that TOI-1266c has retained an H/He atmosphere and thus resides above the radius valley. If that is the case, both of the TOI-1266 planets reside above the radius valley, breaking the underlying assumption of the Owen & Campos Estrada (2020) model of a two-planet system straddling the radius valley. As such, to see if TOI-1266 will be a key test-bed system for testing photoevaporation using this model, a precise measurement of the mass of TOI-1266c is necessary to confirm if it resides above or below the radius valley.

Lastly, we note that during the preparation of this manuscript, we became aware of an independent analysis of this system by Demory et al. (2020). We note that all data analyses and interpretations presented here were performed independently from their work.

7. Summary

We have presented the discovery and validation of two small planets orbiting the nearby M2 dwarf TOI-1266. The inner planet has a radius of 2.5 $R_\oplus$ and an orbital period of 10.9 days. The outer planet has a smaller radius of $R = 1.67\ R_\oplus$ and period of 18.8 days, residing in the radius valley—the transition region between rocky and gaseous planets. From the available photometry and RVs, we see no clear evidence of other planets in the system.

Originally detected in photometric data from the TESS mission, we validate the planetary nature of the two planets using high-contrast imaging observations from NESSI/WIYN, along with ground-based transit photometry, including precision diffuser-assisted photometry of the outer planet using the engineered diffuser on the ARC 3.5 m telescope at APO. Using precision NIR RVs from the HPF, we obtain upper mass limits of 15.9 and 6.4 $M_\oplus$ at 95% confidence for planets b and c, respectively. Our current mass constraints hint that planet c could have a predominantly nonrocky composition, which could indicate that planet c is water-rich and/or has retained an atmosphere despite its small size, although further precise RV observations are needed to more precisely constrain its composition. Given the brightness of the host star, both planets are amenable for a precise mass constraint with current and upcoming RV instruments. A precise mass estimate of planet c will further constrain models explaining the emergence of the radius valley and the processes that sculpt the compositions and atmospheres of small planets receiving insolations similar to Venus.

We thank the anonymous referee for a thoughtful reading of the manuscript and useful suggestions and comments that made for a clearer and stronger manuscript. We thank Josh Winn for useful discussions. This work was partially supported by funding from the Center for Exoplanets and Habitable Worlds. The Center for Exoplanets and Habitable Worlds is supported by the Pennsylvania State University, the Eberly College of Science, and the Pennsylvania Space Grant Consortium. This work was supported by NASA Headquarters under the NASA Earth and Space Science Fellowship Program through grant 80NSSC18K1114. We acknowledge support from NSF grants AST-1006676, AST-1126413, AST-1310885, AST-1517592, AST-1310875, AST-1910954, AST-1907622, and AST-1909506; the NASA Astrobiology Institute (NAI; NNA09-DA76A); and PSARC in our pursuit of precision radial velocities in the NIR. Computations for this research were performed at the Pennsylvania State University's Institute for Computational & Data Sciences (ICDS).

These results are based on observations obtained with the Habitable-zone Planet Finder Spectrograph on the Hobby-Eberly Telescope (HET). We thank the resident astronomers and telescope operators at the HET for the skillful execution of our observations with the HPF. The HET is a joint project of the University of Texas at Austin, the Pennsylvania State University, Ludwig-Maximilians-Universität München, and Georg-August Universität Gottingen. The HET is named in honor of its principal benefactors, William P. Hobby and Robert E. Eberly. The HET collaboration acknowledges support and resources from the Texas Advanced Computing Center.

The WIYN Observatory is a joint facility of the University of Wisconsin–Madison, Indiana University, Yale University, the NSF Optical Infrared Research Lab, the University of Missouri, Purdue University, Penn State University, and the University of California at Irvine. Some of the observations in the paper made use of the NN-EXPLORE Exoplanet and Stellar Speckle Imager (NESSI). NESSI was funded by the NASA Exoplanet Exploration Program and the NASA Ames Research Center. NESSI was built at the Ames Research Center by Steve B. Howell, Nic Scott, Elliott P. Horch, and Emmett Quigley. These results are based on observations obtained with the Apache Point Observatory 3.5 m telescope, which is owned and operated by the Astrophysical Research Consortium. We wish to thank the APO 3.5 m telescope operators for their assistance in obtaining these data. Some observations were obtained with the Samuel Oschin 48-inch Telescope at the Palomar Observatory as part of the ZTF project. The ZTF is supported by the NSF under grant No. AST-1440341 and a collaboration including Caltech, IPAC, the Weizmann Institute for Science, the Oskar Klein Center at Stockholm University, the University of Maryland, the University of Washington, Deutsches Elektronen-Synchrotron and Humboldt University, Los Alamos National Laboratories, the TANGO Consortium of Taiwan, the University of Wisconsin–Milwaukee, and Lawrence Berkeley National Laboratories. Operations are conducted by COO, IPAC, and UW.

We acknowledge the use of public TOI release data from pipelines at the TESS Science Office and the TESS Science Processing Operations Center. This research has made use of the Exoplanet Follow-up Observation Program website, which is operated by the California Institute of Technology, under contract with the National Aeronautics and Space Administration under the Exoplanet Exploration Program. This paper includes data collected by the TESS mission, which are publicly available from the Multimission Archive for Space Telescopes (MAST). Support for MAST for non-HST data is provided by the NASA Office of Space Science via grant NNX09AF08G and by other grants and contracts. This research made use of Lightkurve, a Python package for Kepler and TESS data analysis (Lightkurve Collaboration, 2018). This research made use of the NASA Exoplanet Archive, which is operated by the California Institute of Technology, under contract with the National Aeronautics and Space Administration under the Exoplanet Exploration Program. This work has made use of data from the European Space Agency (ESA) mission Gaia (https://www.cosmos.esa.int/gaia), processed by the Gaia Data Processing and Analysis Consortium (DPAC; https://www.cosmos.esa.int/web/gaia/dpac/consortium). Funding for the DPAC has been provided by national institutions, in particular the institutions participating in the Gaia Multilateral Agreement.

Facilities: TESS, Gaia, HPF/HET 10 m, ARCTIC/ARC 3.5 m, NESSI/WIYN 3.5 m, Perkin 0.4 m, ZTF, ASAS.

Software: AstroImageJ (Collins et al. 2017), `astroplan` (Morris et al. 2018), `astropy` (Astropy Collaboration et al. 2013), `astroquery` (Ginsburg et al. 2018), `barycorrpy` (Kanodia & Wright 2018), `batman` (Kreidberg 2015), `corner.py` (Foreman-Mackey 2016), `celerite` (Foreman-Mackey et al. 2017), `dynesty` (Speagle 2020), `EXOFASTv2` (Eastman 2017), `exoplanet` (Foreman-Mackey et al. 2020), `forecaster` (Chen & Kipping 2017), `GALPY` (Bovy 2015), `GNU Parallel` (Tange 2011), `HxRGproc` (Ninan et al. 2018), `iDiffuse` (Stefansson et al. 2018b), `Jupyter` (Kluyver et al. 2016), `juliet` (Espinoza et al. 2019), `matplotlib` (Hunter 2007), `MRExo` (Kanodia et al. 2019), `numpy` (Van Der Walt et al. 2011), `pandas` (McKinney 2010), `PyMC3` (Salvatier et al. 2016), `radvel` (Fulton et al. 2018), `SERVAL` (Zechmeister et al. 2018), `starry` (Luger et al. 2019), `tesscut` (Brasseur et al. 2019), `transitleastsquares` (Hippke & Heller 2019).

Appendix A
Corner Plots

Figures 10 and 11 show corner plots of the posteriors from our joint fit of the available photometry and radial velocimetry for planets b and c, respectively.

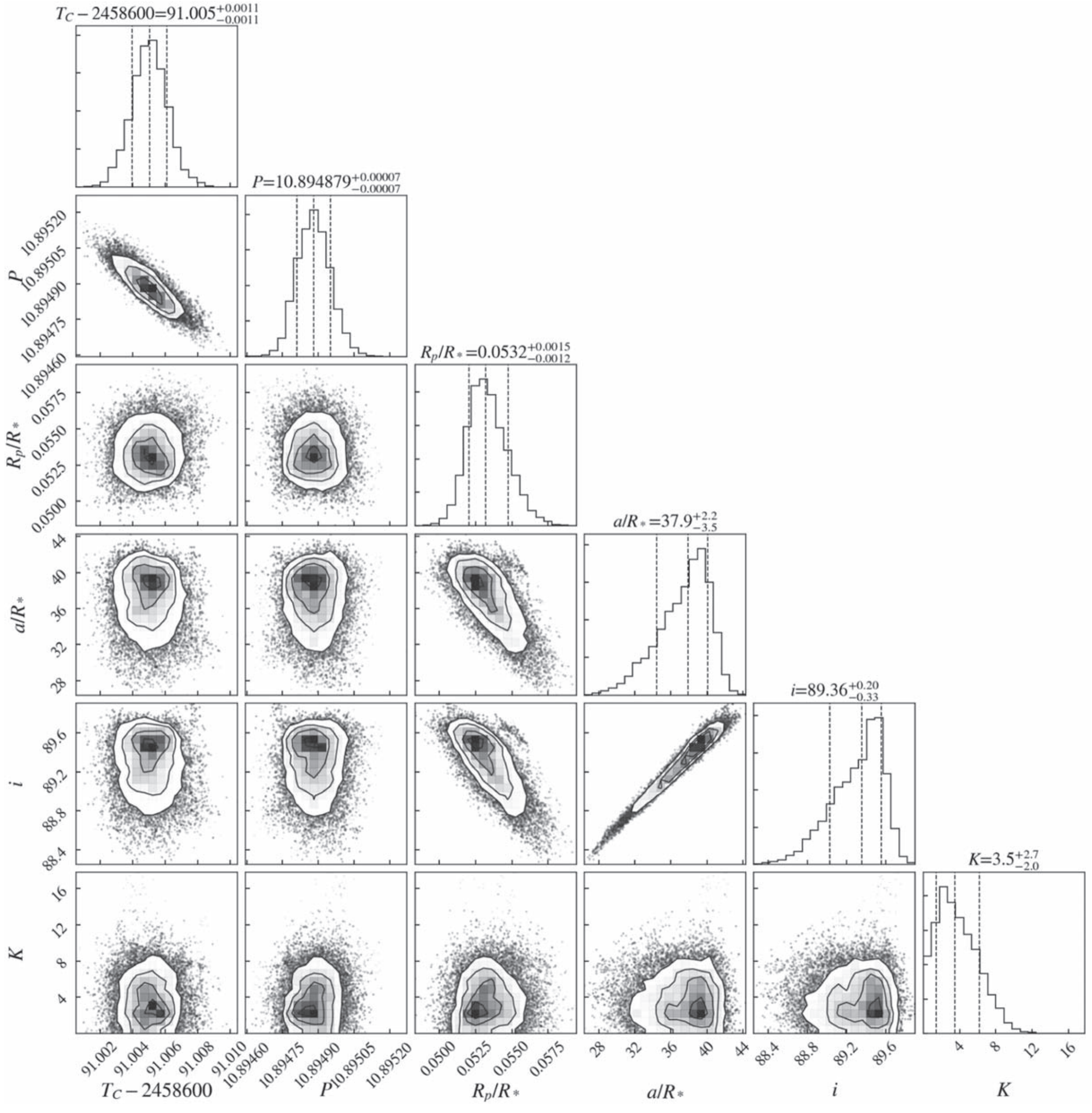

Figure 10. Corner plot of posteriors for TOI-1266b. Plot created with `corner.py`.

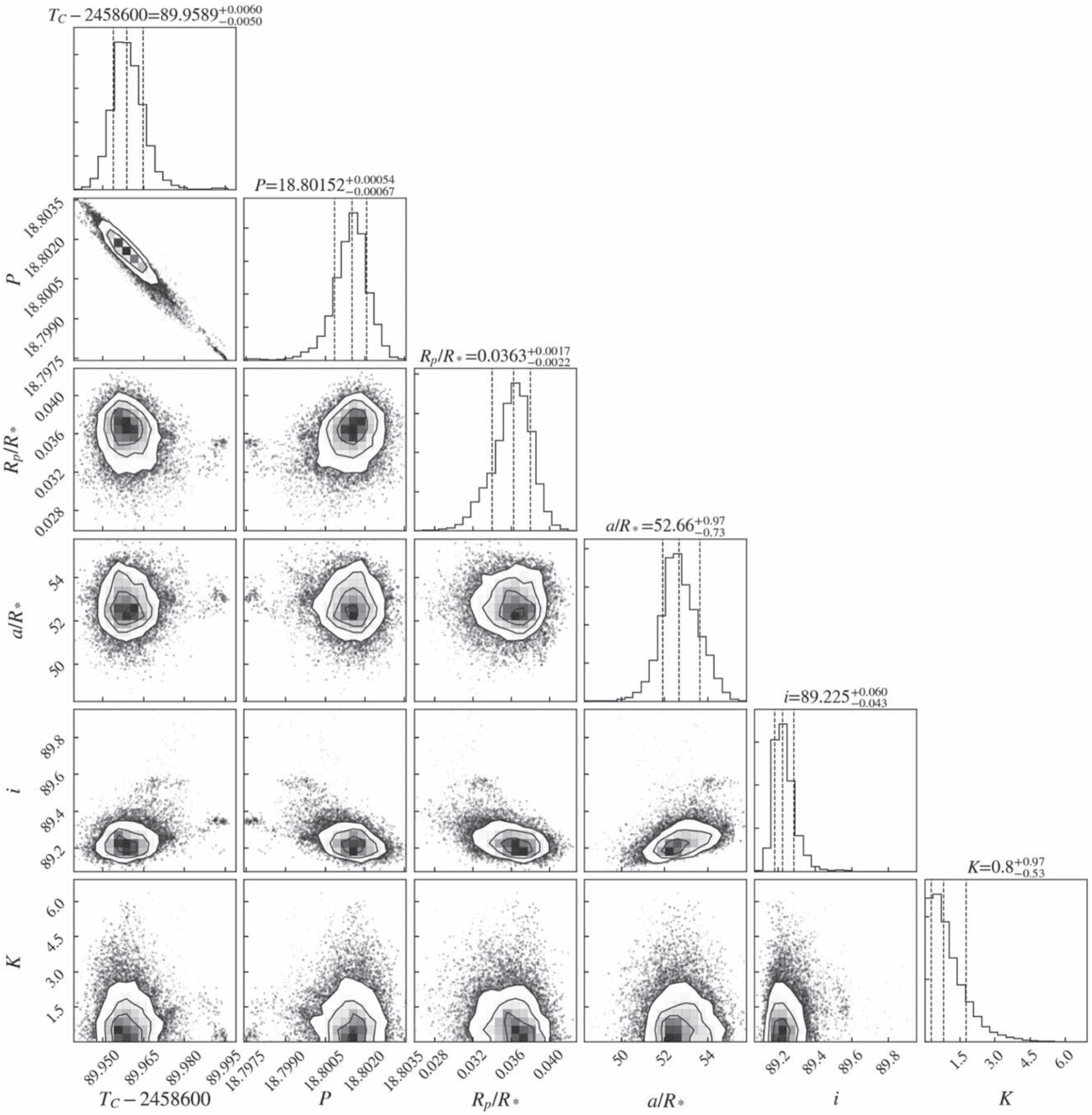

Figure 11. Corner plot of posteriors for TOI-1266c. Plot created with `corner.py`.

Appendix B
HPF Radial Velocities

Table 4 lists the RVs from the HPF and associated activity indicators derived from the spectra used in this work.

Table 4

HPF RVs Used in This Work Along with the dLW, CRX, and Line Indices for the Three Ca II IRT Lines (Ca II IRT 1, 2, and 3) and Associated Errors

BJD	RV [m s^{-1}]	dLW [m^{2}s^{-2}]	CRX [m s^{-1} Np^{-1}]	Ca II IRT 1	Ca II IRT 2	Ca II IRT 3
2,458,854.023,73	−8.7 ± 8.1	69.5 ± 18.9	−205.6 ± 86.9	0.550 ± 0.003	0.308 ± 0.002	0.329 ± 0.002
2,458,859.029,78	−7.9 ± 9.2	−7.2 ± 21.9	290.1 ± 148.0	0.570 ± 0.003	0.308 ± 0.003	0.327 ± 0.003
2,458,861.020,62	1.5 ± 10.8	−4.1 ± 25.4	−178.4 ± 157.4	0.551 ± 0.004	0.298 ± 0.004	0.320 ± 0.003
2,458,868.004,84	−14.9 ± 5.9	21.0 ± 13.8	67.8 ± 77.1	0.570 ± 0.003	0.307 ± 0.002	0.328 ± 0.002
2,458,870.043,13	1.1 ± 11.8	52.6 ± 27.8	211.7 ± 175.4	0.549 ± 0.004	0.306 ± 0.004	0.321 ± 0.004
2,458,882.990,10	17.6 ± 12.5	−29.0 ± 29.3	21.7 ± 212.2	0.562 ± 0.004	0.302 ± 0.004	0.329 ± 0.004
2,458,893.921,90	−8.4 ± 7.4	26.1 ± 17.6	48.1 ± 77.6	0.553 ± 0.002	0.307 ± 0.002	0.336 ± 0.002
2,458,894.924,23	3.8 ± 7.4	19.4 ± 17.6	196.0 ± 121.2	0.562 ± 0.002	0.303 ± 0.002	0.330 ± 0.002
2,458,939.795,00	12.2 ± 7.1	30.4 ± 16.9	−93.4 ± 93.8	0.557 ± 0.002	0.303 ± 0.002	0.327 ± 0.002
2,458,940.828,80	−14.2 ± 10.6	18.7 ± 25.2	−227.9 ± 66.2	0.557 ± 0.003	0.303 ± 0.003	0.339 ± 0.003
2,458,941.804,03	5.9 ± 6.3	23.4 ± 15.1	24.4 ± 94.6	0.557 ± 0.002	0.300 ± 0.002	0.331 ± 0.002
2,458,967.729,65	−4.2 ± 7.1	−13.6 ± 17.0	−217.5 ± 107.5	0.556 ± 0.002	0.297 ± 0.002	0.327 ± 0.002
2,458,969.737,89	−5.0 ± 6.9	21.7 ± 16.7	227.4 ± 62.2	0.554 ± 0.002	0.303 ± 0.002	0.319 ± 0.002
2,458,971.735,16	9.3 ± 7.7	46.1 ± 18.3	−58.6 ± 118.2	0.557 ± 0.002	0.298 ± 0.002	0.317 ± 0.002
2,458,974.752,18	−5.0 ± 6.9	36.8 ± 16.5	45.2 ± 111.3	0.561 ± 0.002	0.300 ± 0.002	0.322 ± 0.002
2,458,975.721,76	15.0 ± 7.9	17.5 ± 18.9	54.5 ± 113.7	0.557 ± 0.002	0.296 ± 0.002	0.326 ± 0.002
2,458,976.716,58	2.2 ± 7.4	39.3 ± 17.8	−40.4 ± 108.5	0.559 ± 0.002	0.305 ± 0.002	0.336 ± 0.002
2,458,978.703,78	9.0 ± 6.4	42.5 ± 15.3	12.6 ± 89.4	0.558 ± 0.002	0.300 ± 0.002	0.337 ± 0.002
2,458,979.695,04	−5.9 ± 6.4	−12.0 ± 15.5	−54.6 ± 118.5	0.561 ± 0.002	0.299 ± 0.002	0.333 ± 0.002
2,459,001.647,72	−0.4 ± 6.7	2.6 ± 16.2	−85.6 ± 45.3	0.553 ± 0.002	0.294 ± 0.002	0.316 ± 0.002
2,459,002.679,16	−12.0 ± 7.5	3.6 ± 18.0	90.5 ± 106.1	0.549 ± 0.002	0.292 ± 0.002	0.312 ± 0.002
2,459,003.646,01	8.1 ± 6.7	−5.4 ± 16.1	65.3 ± 73.3	0.555 ± 0.002	0.293 ± 0.002	0.313 ± 0.002

(This table is available in machine-readable form.)

ORCID iDs

Guðmundur Stefánsson https://orcid.org/0000-0001-7409-5688
Ravi Kopparapu https://orcid.org/0000-0002-5893-2471
Andrea Lin https://orcid.org/0000-0002-9082-6337
Suvrath Mahadevan https://orcid.org/0000-0001-9596-7983
Caleb I. Cañas https://orcid.org/0000-0003-4835-0619
Shubham Kanodia https://orcid.org/0000-0001-8401-4300
Joe P. Ninan https://orcid.org/0000-0001-8720-5612
William D. Cochran https://orcid.org/0000-0001-9662-3496
Michael Endl https://orcid.org/0000-0002-7714-6310
Leslie Hebb https://orcid.org/0000-0003-1263-8637
John Wisniewski https://orcid.org/0000-0001-9209-1808
Arvind Gupta https://orcid.org/0000-0002-5463-9980
Mark Everett https://orcid.org/0000-0002-0885-7215
Chad F. Bender https://orcid.org/0000-0003-4384-7220
Scott A. Diddams https://orcid.org/0000-0002-2144-0764
Eric B. Ford https://orcid.org/0000-0001-6545-639X
Connor Fredrick https://orcid.org/0000-0002-0560-1433
Samuel Halverson https://orcid.org/0000-0003-1312-9391
Fred Hearty https://orcid.org/0000-0002-1664-3102
Marissa Maney https://orcid.org/0000-0001-8222-9586
Andrew J. Metcalf https://orcid.org/0000-0001-5000-1018
Andrew Monson https://orcid.org/0000-0002-0048-2586
Lawrence W. Ramsey https://orcid.org/0000-0002-4289-7958
Paul Robertson https://orcid.org/0000-0003-0149-9678
Arpita Roy https://orcid.org/0000-0001-8127-5775
Christian Schwab https://orcid.org/0000-0002-0091-7105
Ryan C. Terrien https://orcid.org/0000-0002-4788-8858
Jason T. Wright https://orcid.org/0000-0001-6160-5888

References

Adams, E. R., Seager, S., & Elkins-Tanton, L. 2008, ApJ, 673, 1160
Agol, E., Steffen, J., Sari, R., & Clarkson, W. 2005, MNRAS, 359, 567
Akeson, R. L., Chen, X., Ciardi, D., et al. 2013, PASP, 125, 989
Allard, F., Homeier, D., & Freytag, B. 2012, RSPTA, 370, 2765
Alonso-Floriano, F. J., Morales, J. C., Caballero, J. A., et al. 2015, A&A, 577, A128
Anglada-Escudé, G., & Butler, R. P. 2012, ApJS, 200, 15
Astropy Collaboration, Robitaille, T. P., Tollerud, E. J., et al. 2013, A&A, 558, A33
Bailer-Jones, C. A. L., Rybizki, J., Fouesneau, M., Mantelet, G., & Andrae, R. 2018, AJ, 156, 58
Batalha, N. M., Rowe, J. F., Bryson, S. T., et al. 2013, ApJS, 204, 24
Benneke, B., Wong, I., Piaulet, C., et al. 2019, ApJL, 887, L14
Bluhm, P., Luque, R., Espinoza, N., et al. 2020, A&A, 639, A132
Borucki, W. J., Koch, D., Basri, G., et al. 2010, Sci, 327, 977
Bovy, J. 2015, ApJS, 216, 29
Brasseur, C. E., Phillip, C., Fleming, S. W., Mullally, S. E., & White, R. L. 2019, Astrocut: Tools for Creating Cutouts of TESS Images, Astrophysics Source Code Library, ascl:1905.007
Carrillo, A., Hawkins, K., Bowler, B. P., Cochran, W., & Vanderburg, A. 2020, MNRAS, 491, 4365
Chen, J., & Kipping, D. 2017, ApJ, 834, 17
Choi, J., Dotter, A., Conroy, C., et al. 2016, ApJ, 823, 102
Cloutier, R., & Menou, K. 2020, AJ, 159, 211
Cloutier, R., Rodriguez, J. E., Irwin, J., et al. 2020, AJ, 160, 22

Collins, K. A., Kielkopf, J. F., Stassun, K. G., & Hessman, F. V. 2017, AJ, 153, 77

Crossfield, I. J. M., Petigura, E., Schlieder, J. E., et al. 2015, ApJ, 804, 10

Cutri, R. M., Wright, E. L., Conrow, T., et al. 2014, yCat, 2328, 0

Demory, B. O., Pozuelos, F. J., Gomez Maqueo Chew, Y., et al. 2020, A&A, 642, A49

Dittmann, J. A., Irwin, J. M., Charbonneau, D., et al. 2017, Natur, 544, 333

Dotter, A. 2016, ApJS, 222, 8

Dressing, C. D., & Charbonneau, D. 2015, ApJ, 807, 45

Eastman, J. 2017, EXOFASTv2: Generalized Publication-quality Exoplanet Modeling Code, Astrophysics Source Code Library, ascl:1710.003

Eastman, J. D., Rodriguez, J. E., Agol, E., et al. 2019, PASP, submitted (arXiv:1907.09480)

Espinoza, N., & Jordán, A. 2015, MNRAS, 450, 1879

Espinoza, N., Kossakowski, D., & Brahm, R. 2019, MNRAS, 490, 2262

Fischer, D. A., Anglada-Escude, G., Arriagada, P., et al. 2016, PASP, 128, 066001

Fitzpatrick, E. L. 1999, PASP, 111, 63

Foreman-Mackey, D. 2016, JOSS, 1, 24

Foreman-Mackey, D., Agol, E., Ambikasaran, S., & Angus, R. 2017, AJ, 154, 220

Foreman-Mackey, D., Czekala, I., Luger, R., et al. 2020, exoplanet-dev/exoplanet v0.2.6, Zenodo, doi:10.5281/zenodo.1998447

Fressin, F., Torres, G., Charbonneau, D., et al. 2013, ApJ, 766, 81

Fulton, B. J., & Petigura, E. A. 2018, AJ, 156, 264

Fulton, B. J., Petigura, E. A., Blunt, S., & Sinukoff, E. 2018, PASP, 130, 044504

Fulton, B. J., Petigura, E. A., Howard, A. W., et al. 2017, AJ, 154, 109

Gaia Collaboration 2018, yCat, 2345, 0

Gibson, S. R., Howard, A. W., Marcy, G. W., et al. 2016, Proc. SPIE, 9908, 990870

Gillon, M., Triaud, A. H. M. J., Demory, B.-O., et al. 2017, Natur, 542, 456

Ginsburg, A., Sipocz, B., Parikh, M., et al. 2018, astropy/astroquery: v0.3.7 release, Zenodo, doi:10.5281/zenodo.1160627

Ginzburg, S., Schlichting, H. E., & Sari, R. 2016, ApJ, 825, 29

Ginzburg, S., Schlichting, H. E., & Sari, R. 2018, MNRAS, 476, 759

Green, G. M., Schlafly, E., Zucker, C., Speagle, J. S., & Finkbeiner, D. 2019, ApJ, 887, 93

Gupta, A., & Schlichting, H. E. 2019, MNRAS, 487, 24

Hardegree-Ullman, K. K., Zink, J. K., Christiansen, J. L., et al. 2020, ApJS, 247, 28

Henden, A. A., Levine, S., Terrell, D., & Welch, D. L. 2015, AAS Meeting, 225, 336.16

Hippke, M., & Heller, R. 2019, A&A, 623, A39

Holman, M. J., & Murray, N. W. 2005, Sci, 307, 1288

Howard, A. W., Marcy, G. W., Bryson, S. T., et al. 2012, ApJS, 201, 15

Howell, S. B., Everett, M. E., Sherry, W., Horch, E., & Ciardi, D. R. 2011, AJ, 142, 19

Huehnerhoff, J., Ketzeback, W., Bradley, A., et al. 2016, Proc. SPIE, 9908, 99085H

Hunter, J. D. 2007, CSE, 9, 90

Inamdar, N. K., & Schlichting, H. E. 2015, MNRAS, 448, 1751

Jenkins, J. M., Twicken, J. D., McCauliff, S., et al. 2016, Proc. SPIE, 9913, 99133E

Kane, S. R., Barclay, T., & Gelino, D. M. 2013, ApJL, 770, L20

Kane, S. R., Kopparapu, R. K., & Domagal-Goldman, S. D. 2014, ApJL, 794, L5

Kanodia, S., Wolfgang, A., Stefansson, G. K., Ning, B., & Mahadevan, S. 2019, ApJ, 882, 38

Kanodia, S., & Wright, J. 2018, RNAAS, 2, 4

Kaplan, K. F., Bender, C. F., Terrien, R., et al. 2018, in ASP Conf. Ser. 523, Astronomical Data Analysis Software and Systems XXVIII, ed. P. J. Teuben et al. (San Fransisco, CA: ASP), 567

Kempton, E. M. R., Bean, J. L., Louie, D. R., et al. 2018, PASP, 130, 114401

Kipping, D. M. 2013, MNRAS, 435, 2152

Kluyver, T., Ragan-Kelley, B., Pérez, F., et al. 2016, in Positioning and Power in Academic Publishing: Players, Agents and Agendas, ed. F. Loizides & B. Scmidt (Amsterdam: IOS Press), 87, https://eprints.soton.ac.uk/403913/

Kochanek, C. S., Shappee, B. J., Stanek, K. Z., et al. 2017, PASP, 129, 104502

Kopparapu, R. K., Ramirez, R., Kasting, J. F., et al. 2013, ApJ, 765, 131

Kosiarek, M. R., Crossfield, I. J. M., Hardegree-Ullman, K. K., et al. 2019, AJ, 157, 97

Kostov, V. B., Schlieder, J. E., Barclay, T., et al. 2019, AJ, 158, 32

Kovács, G., Zucker, S., & Mazeh, T. 2002, A&A, 391, 369

Kreidberg, L. 2015, PASP, 127, 1161

Lam, K. W. F., Korth, J., Masuda, K., et al. 2020, AJ, 159, 120

Latham, D. W., Rowe, J. F., Quinn, S. N., et al. 2011, ApJL, 732, L24

Lee, E. J., & Chiang, E. 2016, ApJ, 817, 90

Lee, E. J., Chiang, E., & Ormel, C. W. 2014, ApJ, 797, 95

Lépine, S., Hilton, E. J., Mann, A. W., et al. 2013, AJ, 145, 102

Li, J., Tenenbaum, P., Twicken, J. D., et al. 2019, PASP, 131, 024506

Lightkurve Collaboration, Cardoso, J. V. d. M., & Hedges, C. 2018, Lightkurve: Kepler and TESS Time Series Analysis in Python, Astrophysics Source Code Library, ascl:1812.013

Lissauer, J. J., Marcy, G. W., Rowe, J. F., et al. 2012, ApJ, 750, 112

Liu, B., Lambrechts, M., Johansen, A., & Liu, F. 2019, A&A, 632, A7

Liu, S.-F., Hori, Y., Lin, D. N. C., & Asphaug, E. 2015, ApJ, 812, 164

Lopez, E. D., & Fortney, J. J. 2013, ApJ, 776, 2

Lopez, E. D., & Fortney, J. J. 2014, ApJ, 792, 1

Lopez, E. D., Fortney, J. J., & Miller, N. 2012, ApJ, 761, 59

Lopez, E. D., & Rice, K. 2018, MNRAS, 479, 5303

Luger, R., Agol, E., Foreman-Mackey, D., et al. 2019, AJ, 157, 64

Luger, R., & Barnes, R. 2015, AsBio, 15, 119

Mahadevan, S., Ramsey, L., Bender, C., et al. 2012, Proc. SPIE, 8446, 84461S

Mahadevan, S., Ramsey, L. W., Terrien, R., et al. 2014, Proc. SPIE, 9147, 91471G

Mandel, K., & Agol, E. 2002, ApJL, 580, L171

Marcus, R. A., Sasselov, D., Hernquist, L., & Stewart, S. T. 2010, ApJL, 712, L73

Martinez, C. F., Cunha, K., Ghezzi, L., & Smith, V. V. 2019, ApJ, 875, 29

Masci, F. J., Laher, R. R., Rusholme, B., et al. 2019, PASP, 131, 018003

McKinney, W. 2010, in Proc. IX Python in Science Conf., ed. S. van der Walt & J. Millman (Austin, TX: SciPy), 56

Ment, K., Dittmann, J. A., Astudillo-Defru, N., et al. 2019, AJ, 157, 32

Metcalf, A. J., Anderson, T., Bender, C. F., et al. 2019, Optica, 6, 233

Morris, B. M., Tollerud, E., Sipőcz, B., et al. 2018, AJ, 155, 128

Morton, T. D. 2012, ApJ, 761, 6

Morton, T. D. 2015, VESPA: False Positive Probabilities Calculator, Astrophysics Source Code Library, ascl:1503.011

Ninan, J. P., Bender, C. F., Mahadevan, S., et al. 2018, Proc. SPIE, 10709, 107092U

Ostberg, C., & Kane, S. R. 2019, AJ, 158, 195

Owen, J. E., & Campos Estrada, B. 2020, MNRAS, 491, 5287

Owen, J. E., & Wu, Y. 2013, ApJ, 775, 105

Owen, J. E., & Wu, Y. 2017, ApJ, 847, 29

Pepe, F. 2018, Proc. SPIE, 10702, 1

Pepper, J., Gillen, E., Parviainen, H., et al. 2017, AJ, 153, 177

Petigura, E. A. 2020, AJ, 160, 89

Petigura, E. A., Howard, A. W., & Marcy, G. W. 2013, PNAS, 110, 19273

Plavchan, P., Latham, D., Gaudi, S., et al. 2015, arXiv:1503.01770

Quirrenbach, A., Amado, P. J., Ribas, I., et al. 2018, Proc. SPIE, 10702, 107020W

Raymond, S. N., Boulet, T., Izidoro, A., Esteves, L., & Bitsch, B. 2018, MNRAS, 479, L81

Ricker, G. R., Winn, J. N., Vanderspek, R., et al. 2015, JATIS, 1, 014003

Rowe, J. F., Bryson, S. T., Marcy, G. W., et al. 2014, ApJ, 784, 45

Salvatier, J., Wiecki, T. V., & Fonnesbeck, C. 2016, PeerJ Computer Science, 2, e55

Schwab, C., Rakich, A., Gong, Q., et al. 2016, Proc. SPIE, 9908, 054502

Scott, N. J., Howell, S. B., Horch, E. P., & Everett, M. E. 2018, PASP, 130, 054502

Seifahrt, A., Bean, J. L., Stürmer, J., et al. 2016, Proc. SPIE, 9908, 990818

Shetrone, M., Cornell, M. E., Fowler, J. R., et al. 2007, PASP, 119, 556

Smith, J. C., Stumpe, M. C., Cleve, J. E. V., et al. 2012, PASP, 124, 1000

Speagle, J. S. 2020, MNRAS, 493, 3132

Stassun, K. G., Oelkers, R. J., Paegert, M., et al. 2019, AJ, 158, 138

Stassun, K. G., Oelkers, R. J., Pepper, J., et al. 2018, AJ, 156, 102

Stefansson, G., Cañas, C., Wisniewski, J., et al. 2020a, AJ, 159, 100

Stefansson, G., Hearty, F., Robertson, P., et al. 2016, ApJ, 833, 175

Stefansson, G., Li, Y., Mahadevan, S., et al. 2018a, AJ, 156, 266

Stefansson, G., Mahadevan, S., Hebb, L., et al. 2017, ApJ, 848, 9

Stefansson, G., Mahadevan, S., Maney, M., et al. 2020b, AJ, 160, 192

Stefansson, G., Mahadevan, S., Wisniewski, J., et al. 2018b, Proc. SPIE, 10702G, 1070250

Stumpe, M. C., Smith, J. C., Catanzarite, J. H., et al. 2014, PASP, 126, 100

Tange, O. 2011, login: The USENIX Magazine, 36, 42, Zenodo, doi:10.5281/zenodo.16303

Tenenbaum, P., & Jenkins, J. 2018, TESS Science Data Products Description Document, EXP-TESS-ARC-ICD-0014 Rev D, https://archive.stsci.edu/missions/tess/doc/EXP-TESS-ARC-ICD-TM-0014.pdf

Theano Development Team 2016, arXiv:1605.02688

Tsiaras, A., Waldmann, I. P., Tinetti, G., Tennyson, J., & Yurchenko, S. N. 2019, NatAs, 3, 1086
Turbet, M., Ehrenreich, D., Lovis, C., Bolmont, E., & Fauchez, T. 2019, A&A, 628, A12
Twicken, J. D., Catanzarite, J. H., Clarke, B. D., et al. 2018, PASP, 130, 064502
Van Der Walt, S., Colbert, S. C., & Varoquaux, G. 2011, CSE, 13, 22
Van Eylen, V., Agentoft, C., Lundkvist, M. S., et al. 2018, MNRAS, 479, 4786
Van Eylen, V., & Albrecht, S. 2015, ApJ, 808, 126
Weiss, L. M., Marcy, G. W., Petigura, E. A., et al. 2018, AJ, 155, 48
Wright, J. T., & Eastman, J. D. 2014, PASP, 126, 838
Wyatt, M. C., Kral, Q., & Sinclair, C. A. 2020, MNRAS, 491, 782
Yee, S. W., Petigura, E. A., & von Braun, K. 2017, ApJ, 836, 77
Zahnle, K. J., & Catling, D. C. 2017, ApJ, 843, 122
Zechmeister, M., & Kürster, M. 2009, A&A, 496, 577
Zechmeister, M., Reiners, A., Amado, P. J., et al. 2018, A&A, 609, A12
Zeng, L., Jacobsen, S. B., Sasselov, D. D., et al. 2019, PNAS, 116, 9723